Suppression of Premixed Combustion Dynamics Utilizing Microjet Air Injection

by

Duane Edward Hudgins

B.S., University of New Hampshire (2006)

Submitted to the Department of Mechanical Engineering
in partial fulfillment of the requirements for the degree of

Master of Science in Mechanical Engineering

at the

MASSACHUSETTS INSTITUTE OF TECHNOLOGY

June 2008

Author .....
Department of Mechanical Engineering
May 9, 2008

Certified by .....
Ahmed F. Ghoniem
Professor
Thesis Supervisor

Accepted by .....
Lallit Anand
Chairman, Department Committee on Graduate Students

Suppression of Premixed Combustion Dynamics Utilizing Microjet Air Injection

by

Duane Edward Hudgins

Submitted to the Department of Mechanical Engineering
on May 9, 2008, in partial fulfillment of the
requirements for the degree of
Master of Science in Mechanical Engineering

Abstract

The problem of thermoacoustic instability in continuous combustion systems is a major challenge in the field of propulsion and power generation. With the current environmental and political pressure that is being placed on the consumption of fossil fuels, this subject has become even more critical. In the past, the presence of combustion instability could be avoided by designing a combustor with fixed inlet conditions, where these conditions were conducive to a stable system. Today, utilities and providers of propulsion systems are under pressure to make systems that are not only more efficient and clean, but also have a greater flexibility of input fuel. In order to accomplish this, combustion engineers need an even deeper insight into what causes thermoacoustic instability and they need a wider array of tools at their disposal to suppress these instabilities. This thesis adds pieces of that deeper insight and provides another tool to tackle this difficult problem.

As a first step in the further understanding of thermoacoustic instabilities, experiments were done in a premixed gas backwards facing step combustor using propane or propane/hydrogen mixture as a fuel. I fully characterized the combustion dynamics in this combustor by measuring the four defining states of the system. These states are pressure, heat release, velocity, and equivalence ratio. Once these measurements were performed I tested two novel approaches to suppressing thermoacoustic instabilities through the use of microjet air injection. This was done by building upon a previous combustor setup to allow the installation of several new diagnostic capabilities and the new microjets. The new diagnostics include stand-off pressure sensors to measure pressure in the hot exhaust region, a hot wire anemometer to measure velocity, a photomultiplier tube to measure the integrated heat release, an automated gas probe to measure fuel concentration profiles, and a laser absorption sensor to measure the temporal variance in equivalence ratio. The novel microjets were built into the newly designed test section. By fully characterizing the system I was able to show how both equivalence ratio oscillations and wake vortex interactions drive the

thermoacoustic instabilities of the combustion. I have also shown that the stability range shifts to leaner equivalence ratios as inlet temperature or hydrogen content in the fuel is increased. This thesis demonstrates the great potential the microjet air injection has for extending the range of stability of the system.

Thesis Supervisor: Ahmed F. Ghoniem
Title: Professor

Acknowledgments

I would first like to thank Professor Ahmed Ghoniem for his guidance and his belief in me over the past two years. He has pushed me to reach higher and farther in both my research as well as my academic studies.

I would like to thank Professor Anuradha Annaswamy for her guidance and input into this research. I would also like to thank her for the refreshing enthusiasm she would bring to the work, which usually served to drive me into tackling interesting phenomena with renewed vigor.

I want to give a big thank you to both Ray Speth and Murat Altay whom I have learned great deal from and without whom this research would have been exceedingly laborious. I want to also thank them for the companionship they have shown me since I arrived at MIT. Without their presence my experience here would not have been as rich as it has been.

I want to thank my parents, Dean and Christi Hudgins as well as my siblings Darren, Dawn, and Casey for all of their love and support.

This work has been supported by ONR contracts N00014-05-1-0252, and US Department of Energy, University Turbine Systems Research Program, grant DE-FC26-02NT41431. We would like to thank the MIT Edgerton Center for generously allowing use of their high-speed video camera to capture the flame images shown in this paper.

Contents

List of Figures

Chapter 1

Introduction

Combustion instability is a major challenge facing the power generation and propulsion field today. Due to the rising demand of cleaner and more efficient methods of generating power, combustion engineers are under greater pressure to extend the range of stability for combustors. In order to effectively approach this problem one is first required to have a thorough understanding of the dynamics that lead to thermoacoustic instabilities in premixed gas combustors. This understanding is cultivated through the intelligent use of diagnostics such velocity probes, pressure sensors, equivalence ratio sensors, video etc. Understanding combustion dynamics enables the engineer to make educated design decisions, especially when there is a need to implement passive control strategies. Passive controls strategies are able to suppress thermoacoustic instabilities in premixed combustors by disrupting the coupling mechanisms that feed these instabilities. In this thesis the injection of air through micro-sized holes is explored as a possible passive control strategy over thermoacoustic instability.

1.1 Current Challenges

The problem of thermoacoustic instability in premixed gas combustion is not a new subject. With the current environmental and political pressure that is being placed

on the consumption of fossil fuels, this subject has become even more critical [1]. In the past, the presence of combustion instability could be avoided by designing a combustor with fixed inlet conditions, where these conditions were conducive to a stable system [2].

Due to the changing supply of fossil fuels combustion designers are having to design combustors that are more flexible in terms of the fuel source. This need for flexibility is clearly seen in the development of Integrated Gasification Combined Cycle (IGCC) plants. IGCC plants operate by gasifying coal first and then burning the gases in a lean premixed gas combustor. The product gas from the gasification is mostly a mixture of CO and H_2 and is called syngas, which is short for "synthetic gas". This generation cycle is advantageous, because of the lower NO_x and SO_x emissions and IGCC plants can be retrofitted for carbon capture. IGCC plants also have higher efficiency [3].

The greater the flexibility of an IGCC plants choice of hydrocarbon, the more economical the plant will become. Plant flexibility in the choice of hydrocarbon is an issue, because coal will have a different composition depending on where it is mined from. This means that when the coal is gasified the syngas will have a different composition of the two primary gases of H_2 and CO. If the IGCC plant has a wider range of operable syngas compositions, then the plant will be able to choose a more cost-effective coal to burn at a given time. Depending on the current market the IGCC plant could also run off of other hydrocarbons, such as natural gas or biomass [1]. This need for versatility in the fuel translates immediately to the need for versatility in the combustion. The combustor will need to remain stable under a range of fuel concentrations and equivalence ratios. It is here that the need arises for knowledge of how to suppress combustion instabilities.

1.2 Thermal Acoustic Instability

Continuous combustion systems common in these power generation and propulsion applications are susceptible to thermoacoustic instability, which typically occurs under lean burn conditions, where most emissions and efficiency benefits are achieved and near stoichiometry, where high power density is the objective. As a result of the resonant interactions between driving heat release mechanisms and feedback acoustic modes, these combustors are known to exhibit significant pressure and flow oscillations, which may cause flame extinction, structural vibration, flame flashback and even structural damage [4, 5]. Several mechanisms appear to be present in a combustor that instigate and promote such interactions: flame-acoustic wave interactions, flame-vortex interactions, equivalence ratio fluctuations, flame wall interactions and the effect of unsteady stretch rate, all of which may be present individually or simultaneously [6, 7, 8].

Due to the consequences mentioned above combustion instability is unacceptable in most combustors. Other consequences of combustion instability include the production high levels of noise, possible component melting, an increase in emissions and high heat transfer rates [9]. In premixed gas combustors the fundamental mechanism which drives thermal-acoustic instability is described by the Raleigh Criterion. This criterion models a one-dimensional combustor and states that when there are both heat release oscillations and acoustic oscillations present, the heat release oscillations will give a positive gain to the pressure oscillations when the two are $\pm 90^o$ in phase with each other. This relation is shown here

$$\int_0^\tau \int_V p'(x,t)q'(x,t)dVdt > \int_0^\tau \int_V \Phi(x,t)dVdt \tag{1.1}$$

where p'(x,t) are pressure perturbations, q'(x,t) are heat release perturbations, $\Phi(x,t)$ is the wave energy dissipation, V is the control volume (the combustor volume)

and τ is the period of oscillation [10].

1.3 Characterizing Combustion Dynamics

In order to know the full state of the premixed gas combustion process one needs to know the four simultaneous states of the system. These four parameters are pressure (p), heat release (q), velocity (u), and equivalence ratio (ϕ). The most complete account of these parameters would require a measurement of each of these through the entire volume of the combustor at each instant in time, but for this thesis perturbations of these parameters are taken from either point measurements or integrated measurements at the combustion region.

By measuring these parameters one is able to come to a more thorough understanding of the mechanisms that lead to combustion instabilities. The two mechanisms that I will explore in this thesis are the flame-vortex interactions and the equivalence ratio oscillations (denoted as ϕ'), which are the most significant instability mechanisms in large scale gas turbine combustors [11, 12]: i) *Flame-vortex interactions* - As a result of the interaction between the flame and the large vortex formed downstream of the dump plane, the heat release rate oscillates significantly. The heat release rate rises as the flame starts its convolution around the new formed vortex and continues to rise as the vortex grows. After the vortex reaches its maximum size, the leading edge of the flame folds, trapping pockets of reactants. As the pocket is consumed, a combustion pulse is produced, creating large amount of small-scale turbulence and flame surface area. When the periodic heat release supported by the flame-vortex interaction as described couples positively with the acoustic pressure field, self-sustained acoustic oscillations are formed. The acoustic oscillations (p') are directly correlated to velocity oscillations (u'), which effects the shear layer at the step thereby coupling the vortex shedding frequency to these acoustic oscillations

[12, 13, 14, 15, 16, 17, 18, 19, 20]; ii) *Equivalence ratio oscillations* - Equivalence ratio oscillations couple pressure oscillations to heat release oscillations by creating flow rate variations in either the fuel line, the main air line or both. If the fuel line is not fully choked, then the pressure oscillations in the combustor will mean a variation in the driving pressure within the fuel supply line, leading to noticeable oscillations in the fuel flow rate. Also, the velocity oscillations at the fuel supply modulates the air flow rate. Both the oscillations in fuel and air flow rates result in equivalence ratio fluctuations at the location of the fuel injector. The equivalence ratio of a premixed fuel/air mixture is only temporally uniform when both the air and the fuel are mixed at a constant rate. When either flow rate deviates the equivalence ratio will deviate. These oscillations convect through the flame zone where it directly effects the burning speed of reactants and the heat of reaction of the mixture causing heat release rate oscillations. If heat release rate oscillations couple positively with the acoustic pressure field, then self-sustained oscillations are formed [21, 22, 23, 24].

1.4 Effects of Inlet Parameters on Dynamics

Recently, in order to broaden the operating range of the combustors, hydrogen enriched hydrocarbons are used as fuels in LPP combustors [25, 26, 27, 28]. Hydrogen enrichment lowers the flame temperature which helps reducing NO_x emissions and reduces the flammability limit of the combustor. Observed combustion dynamics and flame structures are also impacted by hydrogen enrichment as a result of its influence on reaction kinetics. The impact of inlet temperature on thermoacoustic instabilities, flame structure and flammability limits have also been investigated and noticeable shifts in regions of unstable combustion have been observed [29, 30]. In this thesis, I carry out a parametric study in an atmospheric backward facing step combustor to identify the relative contributions of different mechanisms on thermoacoustic insta-

bility and flame dynamics and to investigate the effects of equivalence ratio, Reynolds number, inlet temperature and the fuel composition on combustion dynamics. Extensive instrumentation of the combustor allows monitoring of temporal variations in pressure, heat-release, and flow velocity, as well as temporal and spatial variations in equivalence ratio.

I fired the combustor at Reynolds numbers of 6500 and 8500 based on the step height using pure propane or propane enriched with hydrogen by adding 2.0% by mass (30% by volume; 4.8% by LHV) or 4.4% by mass (50% by volume; 10.6% by LHV) hydrogen. At each fuel composition and Reynolds number, I varied the equivalence ratio of the fuel-air mixture from near the lean blow-out limit to a value approaching the flashback limit. The inlet mixture is heated to temperatures as high as 600 K. I conducted these experiments with the fuel injector located 28 cm or 93 cm upstream of the step. The fuel injector location effects combustion dynamics since it impacts air-fuel premixing, amplitude of equivalence ratio oscillations, and the convective time scale [23]. By modifying the equivalence ratio oscillations reaching the combustion zone, I determine the relative contributions of flame-vortex interactions and equivalence ratio oscillations on thermoacoustic instability.

1.5 Microjet Control Strategies

Apart from the need to understand the mechanisms that lead to combustion instability there is also a great need for practical passive control strategies for premixed combustors which are able to extend the stable range of operation. The potential for suppressing combustion instability by injecting air through micro-sized holes (known as microjets) has been shown in the past [31, 32]. Most of the work that has been done involving combustion control with microjets has been with the injection of reactive fuels such as hydrogen [33, 34]. In this thesis the potential for microjets to

expand the stability range for a backwards facing step combustor will be explored. In each configuration there is a row of 12 microjets equally spaced and aligned across the span of the combustor. The holes are each 500 μm in diameter. The intended advantage of the microjet approach is that the air being injected through them is choked and therefore the flow rate of the jet is not coupled to the acoustics of the combustor. The other intended advantage is that the microjets are meant to alter the velocity field/disrupt boundary layers and by choking the air, that air is injected into the main flow at near sonic speeds. This translates to injecting the highest amount of momentum with the least amount of secondary air flow. The disadvantage to this process is the need for a secondary air source with a pressure that is high enough to choke across the microjet holes. This source pressure needs to be at least twice the downstream pressure, which would be the pressure of the combustion region that the microjets are injecting into.

There are two configurations of these microjets that will be explored. Both rows of microjet will be located near the tip of the step. The first configuration that will be experimented with is a row of microjets arrayed along the top edge of the step. This row is positioned here with the intent of disrupting the boundary layer which has developed upstream of the step and is the main source of wake vortex shedding. The second configuration is an array of microjets located along the edge of the step tip on the other side, on the backwards face of the step. These microjets are positioned with the intent of disrupting the vortex dynamics as they propagate downstream from the step. The effects of each of these configurations will be analyzed to see which are more or less effective at suppressing combustion instabilities for relevant input conditions.

1.6 Overview of the Thesis

This thesis is broken into four chapters, which are the Introduction, Experimental Setup, Results and Conclusions. Before each chapter is a brief summary of what is covered in that chapter. Chapter 1 is the introduction and it is self-explanatory. Chapter 2 covers the experimental setup and the several new diagnostics installed in the setup to accomplish this work. These new diagnostics include a gas probe to measure the *spatial* fuel concentration, a laser absorption sensor to measure the *temporal* variance in fuel concentration, pressures sensors that can be mounted at high temperature regions, a hotwire anemometer for point measurements of velocity and a photomultiplier tube for integrated heat release measurements. The final section of chapter 2 describes the modifications to the main section that allow the installation of these diagnostics and it describes the design of the new microjet injectors.

Chapter 3 covers the wide body of results explored for this work. The first set of results are the spatial measurements of fuel concentration and velocity on planes perpendicular to the flow. Results detailing the behavior of the combustion dynamics are explored in depth. This includes observed hysteresis effects on stability conditions, the effects on the dynamics of fuel injection location, hydrogen addition, Reynolds number and inlet temperature as well as the high speed video of the flame dynamics. The final section of chapter 3 details the effects of the normal and axial microjets on the combustion dynamics and their ability to suppress thermoacoustic instability.

Chapter 4 covers the main points to be taken away from the thesis and the conclusions drawn from the overall work. This includes a summary of the different combustion modes, the overall effects varied parameters have on the combustion and the conclusions drawn about the influence of microjet air injection on the combustion dynamics.

Chapter 2

Experimental Setup

The Reacting Gas Dynamics Laboratory's backwards facing step combustor was on its second design iteration before I started the work for this thesis. I found that the setup was too limited in its diagnostic access to be able to accomplish the goals for this work. The design was also not malleable enough to implement the new microjet injection strategy. Due to these conditions I was required to redesign the main combustor test section, which is the section of the combustor from the ramped contraction to the area directly downstream of the step. The modifications to the design included several new diagnostic integrations to measure equivalence ratio, velocity, pressure, and heat release. The side windows at the step section were widened substantially to allow greater visual access. The fuel injectors 28 cm upstream of the step were redesigned to achieve the appropriate amount of premixing for fuel injection at that location. The step corner was redesigned for the implementation of new microjet injection strategies.

2.1 Overall System

Figure 2-1 shows a schematic diagram of the rearward-facing step combustor. The combustor consists of a rectangular stainless steel duct with a cross section 40 mm

high and 160 mm wide. The air inlet to the combustor is choked. 0.45 m downstream from the choke plate, a 0.15 m long ramp contracts the channel height from 40 mm to 20 mm followed by a 0.4 m long constant-area section that ends with a sudden expansion back to 40 mm. The step height is 20 mm. The overall length of the combustor is 5.0 m. A circular exhaust pipe comprises the last 3.0 m of the combustor. The combustor is equipped with quartz viewing windows. An air compressor supplies air up to 110 g/s at 883 kPa. A pair of Sierra C100M mass flow controllers allow arbitrary propane/H_2 mixtures at maximum flow rates of 2.36 g/s for propane and 0.30 g/s for hydrogen.

Fuel is injected through several spanwise holes in a manifold located 93 cm upstream of the step, or through microjets from top and bottom walls of the combustor located 28 cm upstream of the step. Secondary air could be injected from 12, 500 μm diameter choked microjets drilled along the combustor width in the cross-stream direction 5 mm upstream of the step, or in the streamwise direction near the corner of the step. Images of the flame are captured using a Phantom v7.1 high-speed camera and used to examine the combustion dynamics. Pressure measurements are obtained using Kulite high intensity microphones designed for laboratory investigations. The flow velocity is measured using TSI IFA300 hotwire anemometer. The temporal equivalence ratio variations are measured 14 cm upstream of the step using a Hamamatsu P4245 photodiode to detect absorption of a HeNe laser by propane. This laser is modulated using a Scitec Instruments 360 OEM optical chopper. The inlet temperature is adjusted using an Osram Sylvania 18 kW in-line electric heater with on/off temperature controller. The spatial concentration measurements are performed under non-reacting flow conditions by injecting CO_2 into the combustor (as a fuel surrogate) together with air and taking point measurements of its concentration. The point measurements are taken over a planar cross section at the location of the step and the gas samples are analyzed using a California Analytical Instruments ZRH

CO/CO_2 analyzer. All data is acquired using a National Instruments PCIe-6259 data acquisition board and the Matlab Data Acquisition Toolbox. A custom Matlab code is used to store the data and control the experiment.

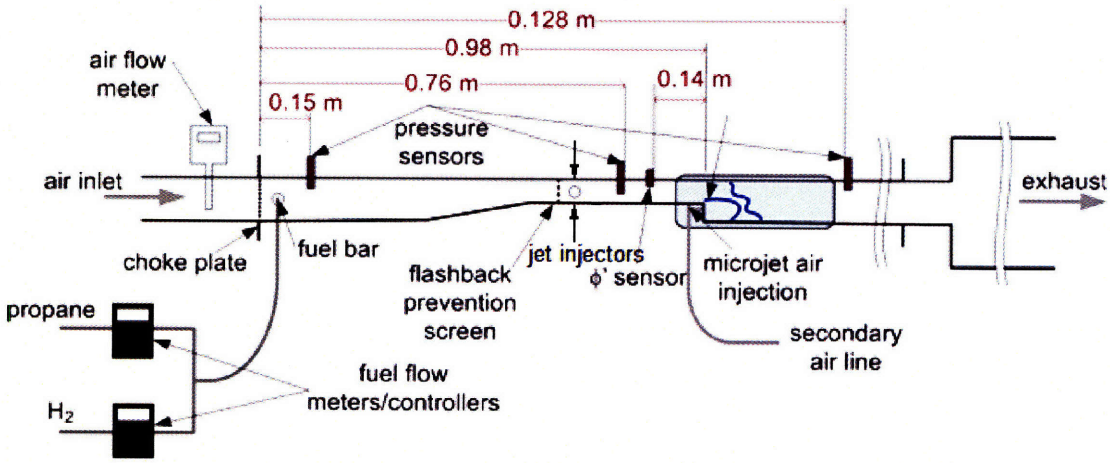

Figure 2-1: The schematic of the overall experimental combustor setup.

2.2 New Diagnostic Capabilities

One of the major goals of this thesis was to fully characterize the combustion process through measurement of the four defining parameters of the system. At the beginning of this work the diagnostic capabilities of the experiment were limited to three pressure sensors located within the first meter of the combustor length, a photodiode array for the measurement of heat release, and a high-speed camera. The high speed camera was very useful, but the quartz viewing window was too narrow which meant that it was not possible for many cases to record the full dynamics of the flame front. In order for me to reach my first goal of complete characterization of the combustion, I was required to build and improve upon the existent experimental setup and its diagnostic capabilities.

2.2.1 Spatial ϕ

In order to inject fuel close to the combustion zone whilst still maintaining two-dimensional dynamics, I needed to measure the level of spatial variation in the fuel concentration entering the combustion zone. I decided to implement this by taking point measurements of the fuel concentration on a plane perpendicular to the direction of the flow in the duct. This involved mounting a gas probe to two automated platforms (shown in figure 2-2). The automated platforms allowed me to digitally program the sampling path and the duration of samples for the probe. They were digitally controlled from serial commands that were issued from the main Matlab program.

In order to measure the concentration profile I decided to use carbon dioxide as a surrogate for propane in order to minimize the risks associated with conducting these experiments with unburned reactive fuel. To simulate the equivalent fuel concentration of propane with the fuel surrogate, I equated the volume flow rate of the surrogate with that of the required flow rate of propane to get the target equivalence ratio. The probe measured the point concentration of the surrogate in molar concentration of $CO_2(x_{CO_2})$. The conversion to equivalence ratio was done using this equation

$$\phi = \frac{5\beta x_{CO_2}}{1 - x_{CO_2}} \tag{2.1}$$

where ϕ is the equivalence ratio, x_{CO_2} is the measured molar concentration of the CO_2,and $\beta = 4.76$ and is the number representing the balance between oxygen and nitrogen in air.

In order for the probe to be inserted into the flow a plexiglass window was made with a slot as shown in figure 2-3. Measurements were taken with a angled probe and with a straight probe. The angled probe took measurements 1 cm upstream of the

expansion. The straight probe took measurements 2 cm downstream of the expansion in order to measure the effect of microjets.

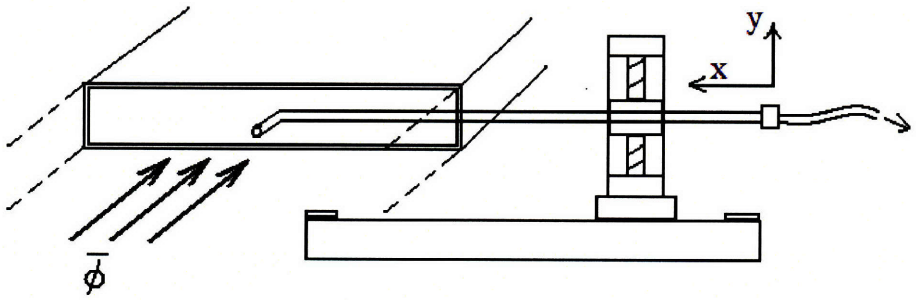

Figure 2-2: The schematic of the traversing probe setup. The gas probe is a tube that is either *bent* into the flow or *straight* and mounted to two automated platforms that control x,y position.

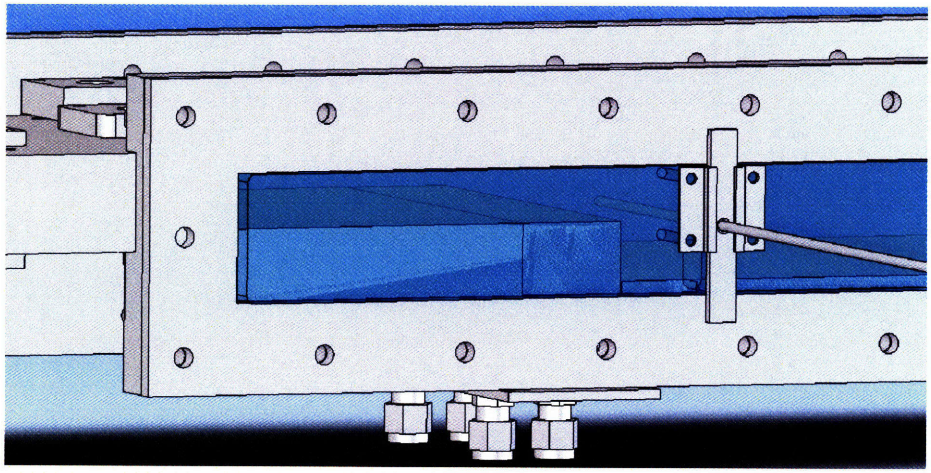

Figure 2-3: A schematic representation of the slot window with the gas probe inserted. This is the configuration utilized to measure the spatial ϕ and $\overline{u}$ 2 cm downstream of the step shown in figure 3-5.

2.2.2 Temporal ϕ

The equivalence ratio is measured during combustion using a laser absorption sensor shown in figure 2-4. The equivalence ratio is found by measuring the reduction in

the intensity of laser light passing through the combustor using a Hamamatsu P4245 light sensor, which is referred to here as the laser intensity sensor. The laser emits light at a wavelength of 3.39 μm, which is within the absorption band of propane. In this device there are three sources of noise that effect the measurement. The first source is the drifting variation in the output intensity of the laser. The second is the light from the flame that the laser intensity sensor senses when the flame gets close to the laser window. The third source of noise is the drift that can occur in the laser intensity sensor when the combustor starts to radiate heat. The laser intensity sensor's sensitivity reduces as its casing increases in temperature.

To overcome these noise issues I first installed a CaF2 50/50 beam splitter and another light sensor. The beam splitter directed half of the beam into the combustor and the other half of the beam was directed to a separate sensor, which is referred to here as the reference sensor. The reference sensor enabled me to account for the variation in the laser power with time. I also installed a high frequency beam chopping wheel to modulate the laser signal. By modulating the laser signal it was now possible to discriminate between laser light and light from the combustor and to filter out the latter. In order to mitigate the effects of the hot combustor on the laser intensity sensor's sensitivity I mounted the sensor 50 cm away from the combustor to minimize the heat transfer between the two. The laser intensity sensor was also mounted to a reflective aluminum mount, which shielded the sensor casing much more effectively than the sensors stock black housing.

The signal processing for the equivalence ratio measurement was done by first finding the %Reduction in the laser intensity from absorption by the fuel using the transfer function

$$\%Reduction = \left(1 - \frac{I_s}{I_{ref}A}\right) \cdot 100\% \tag{2.2}$$

Where I_s is the magnitude of the laser intensity sensor signal and I_{ref} is the

magnitude of the reference sensor signal. The value A is a scaling constant that is determined before each sampling case by recording the signals without fuel being added to the main flow. A is calculated using

$$A = \frac{I_{s,\phi=0}}{I_{ref}} \tag{2.3}$$

The scaling constant A is the base magnitude relation between the two sensors. This constant can vary depending on the temperature of the room, the alignment of the optics, etc. It is measured before each case rather than only once to reduce the possible contribution of these errors.

The temporal ϕ sensor is calibrated by acquiring a calibration curve between ϕ and %Reduction. The calibration is performed by injecting a propane/air mixture at a particular ϕ far upstream of the step, so that the fuel mixture will be homogeneous at the sensor window, and recording %Reduction. This calibration curve can be used to measure the equivalence ratio regardless of the flow rate. The combustion chamber is at atmospheric pressure and the absorption sensor only measures the molar concentration of the propane in the chamber. Looking simply at conservation of mass, there will always be a fixed amount of propane occupying the volume of the combustion chamber that is set by the equivalence ratio. Increasing the flow rate of the mixture will increase the mass flow rate of the propane, but it will not change the amount of propane occupying the volume and therefore the measurement will not be effected.

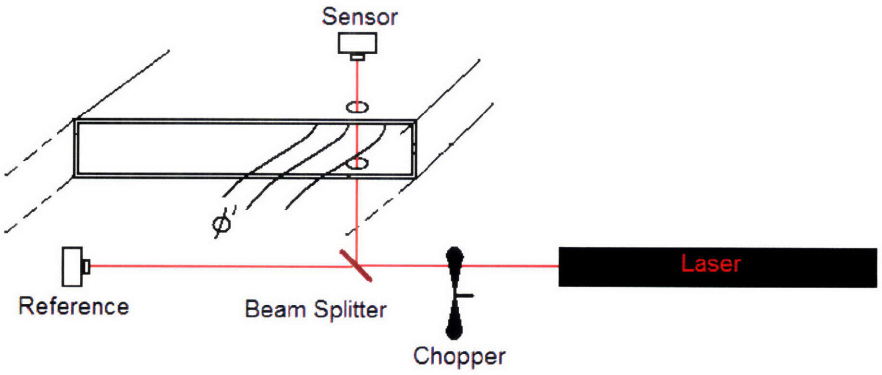

Figure 2-4: The schematic of the laser absorption sensor. The laser window is located 14 cm upstream of the step expansion.

2.2.3 Pressure Sensors

Pressure is measured downstream of the combustor using Kulite MIC series high intensity microphones. These microphones cannot tolerate direct exposure to the exhaust heat so the semi-infinite tube method of mounting the pressure sensors was used as shown in figure 2-5. In order to assure that the acoustic oscillations were dampened I chose a length of tubing 100' long. The pressure sensors were mounted along the length of the combustor at the locations shown in figure 2-6. These sensors were positioned in order to verify the shape of the dominant acoustic wave mode as will be seen in Chapter 3.

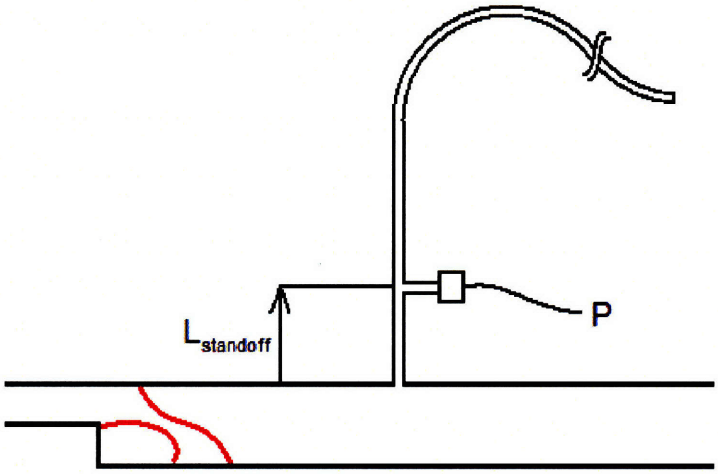

Figure 2-5: The schematic of the pressure sensor mount utilizing the semi-infinite tube method. This pressure sensor mount is capable of being mounted at high temperature regions.

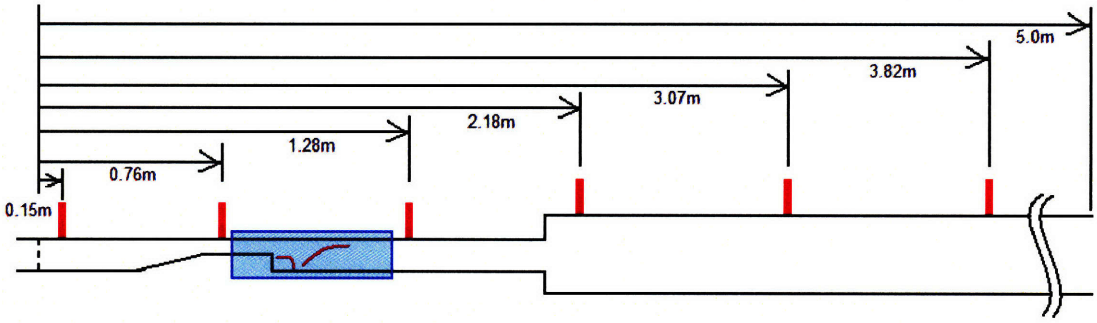

Figure 2-6: The mount positions of the pressure sensors along the length of the combustor. This array of pressure sensors provides a means of measuring the acoustic wave mode of the combustor.

2.2.4 Hot Wire Anemometer

A TSI IFA300 hot wire anemometer was used to take velocity measurements within our combustor. The first use for the hot wire anemometer was the measurement of the instantaneous velocity during combustion. The probe was inserted into the combustor 76 cm downstream of the inlet. The hot wire anemometer is excited with a constant

current source. The voltage across wire is measured using an AD623 instrumentation amplifier. The probe was calibrated by inserting it into the duct at its location 76 cm from the inlet. The flowrate in the experimental duct was varied between 0-15 m/s and the voltage was measured over the range. The resulting calibration curve has less than 10% error, which is adequate for the needs of this research since the *phase* of the velocity oscillations is of primary importance. The anemometer probe was also attached to the automated traversing platforms shown in figures 2-2 and 2-3 to allow the spatial distribution of the *magnitude* of velocity to be measured downstream of the step.

2.2.5 Photomultiplier Tube

I used a Hamamatsu H9306 photomultiplier tube (PMT) to measure the phase of the overall heat release of the combustion. It uses a 430 nm optical bandpass filter to allow it to measure only light emitted from the CH* chemiluminescent reaction that takes place during combustion. The chemiluminescence of the decaying CH radical in the flame front has been directly correlated to the magnitude of the heat release [35, 36]. Since the PMT has no lens it takes an integrated measurement all light sources within its field of view that is at a wavelength of 430 nm as shown in figure 2-7.

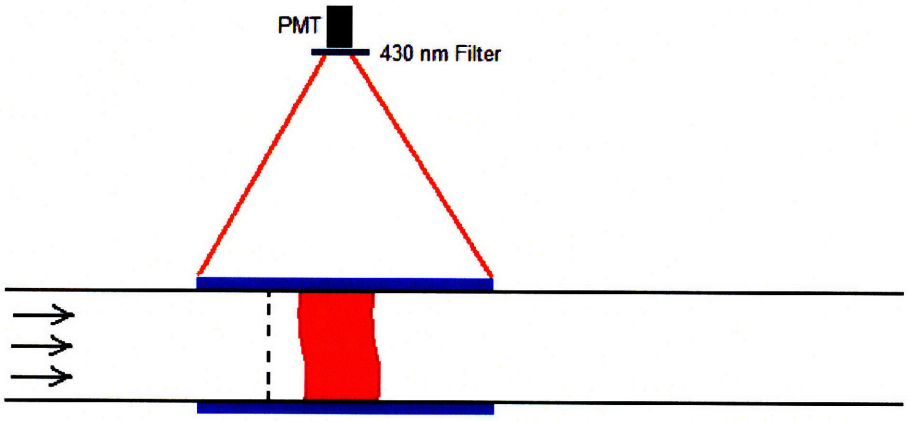

Figure 2-7: The position of the photomultiplier tube with a 430 nm optical bandpass filter. The integrated light that this sensor sees is used as a measurement of heat release.

2.2.6 New Step Section

A new test section was designed for the step combustor to allow for the several new approaches I took with this research. The comparison between the old and new setup can be more clearly seen in figures 2-8 and 2-9. The first substantial improvement was the lengthening of the combustor side window by 8 in. This allowed a full capturing of the flame dynamics with high speed video, which was not possible with the previous setup. A new design for the fuel injection also proved to be crucial to getting relevant results.

The new fuel injectors are shown in figure 2-10 and differ from the older holed fuel bars shown in figure 2-11. The new fuel injector design is only necessary for the fuel injection close to the step since the convective time scale is too short to allow complete diffusion between the fuel and the air. They are mounted such that the fuel is injected from holes 500 μm in diameter. These holes are located on the top and bottom walls of the combustor. The major flaw in the holed fuel bars was the stagnation pressure that forms at the closed tip of each fuel bar. This translates to a

pressure gradient along the length of the combustor and consequently a gradient in the injection velocity of the fuel as shown in figure 2-12. The new fuel injectors reduce the effect of stagnation pressure points by first having two inlets for each manifold as seen in figure 2-10. One can get a feeling for the resulting flow profile for the micro-sized fuel injectors in figure 2-13. The effect of this new fuel injection manifold will be seen in section 3.1.

The microjet injectors have also been modified to allow for the exploration of two new microjet locations, which are termed the "normal microjets" and the "axial microjets" where the names correspond to their locations. This is clear to see in figure 2-14. The new design of the step allows a much easier exploration of new injection locations compared to the old step configuration. The corner of the step was redesigned such that it is easily interchangeable, should new controller designs be implemented. With the new design the step corner becomes the manifold for both microjet configurations and is shown in figures 2-15 & 2-16. The new method that I discovered was the use of microjets in the axial direction as shown in figure 2-14 and is shown on the new manifold in figure 2-15. The microjets are also capable of injecting air in the normal location at two locations upstream of the expansion as shown in figure 2-16.

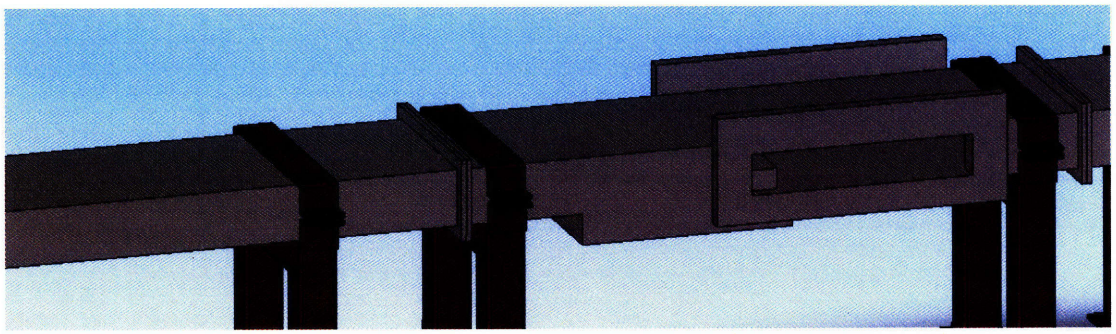

Figure 2-8: The version of the backwards facing step combustor test section before it was redesigned. The viewing window was much narrower and there were fewer ports for diagnostics. It was also not possible to modify it for testing the new microjet schemes.

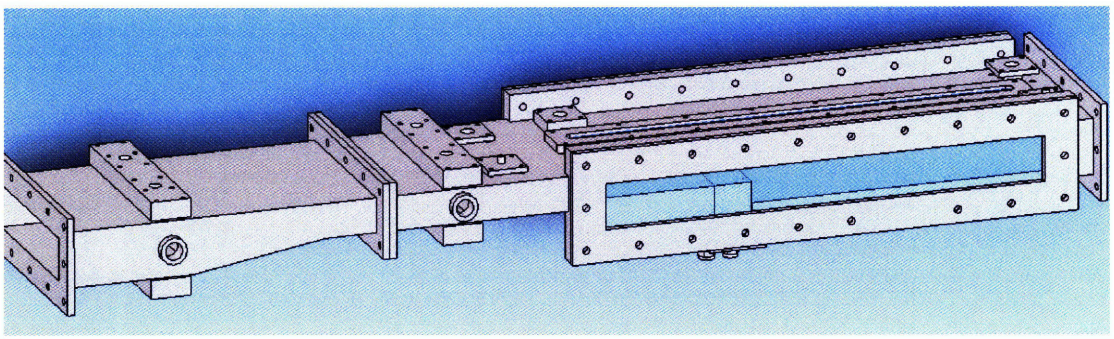

Figure 2-9: The redesigned step combustor test section which provides a wider viewing range and multiple interchangeable diagnostic ports. The new step manifold design allows for testing new and future microjet injection methods.

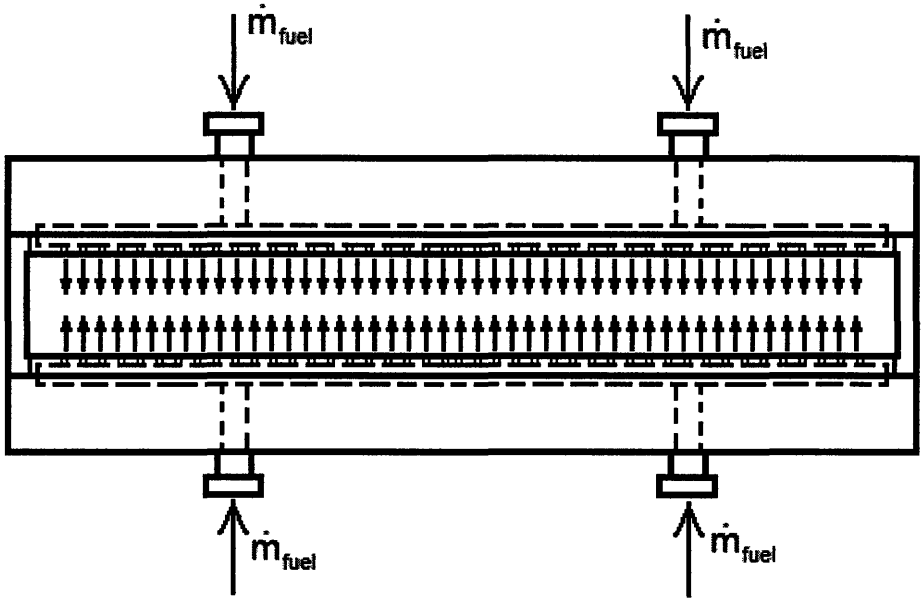

Figure 2-10: A sliced spanwise cross-section of the microjet fuel injectors located 28 cm upstream of the step.

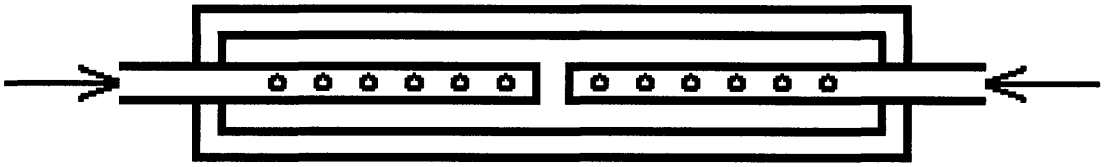

Figure 2-11: A sliced spanwise cross-section of the old fuel manifold design still utilized for injection at the 93 cm location.

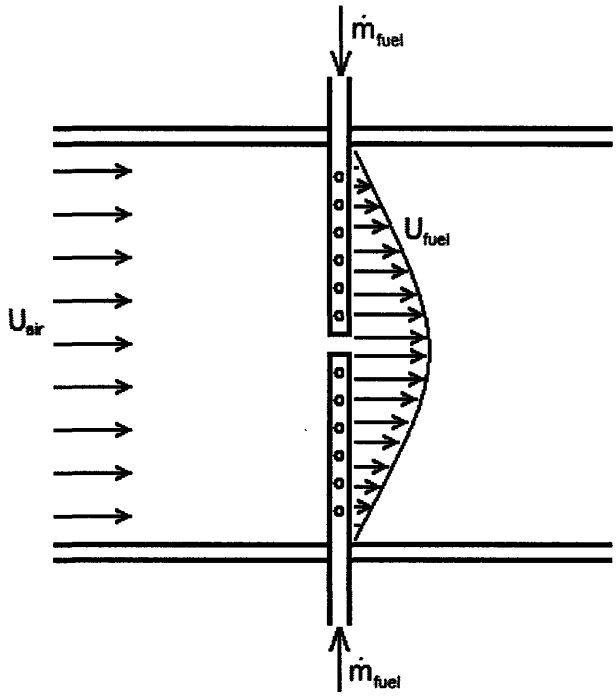

Figure 2-12: A schematic representation of the injected fuel velocity profile with the old holed tube fuel injectors. The cross-section is sliced through a plane parallel to the top and bottom walls of the duct.

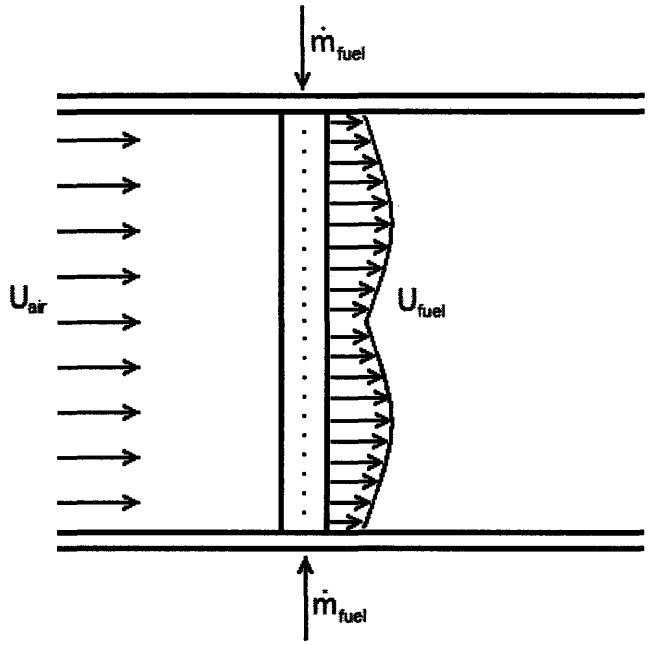

Figure 2-13: A schematic representation of the injected fuel velocity profile with the new micro-holed fuel injectors. The cross-section is sliced through a plane parallel to the top and bottom walls of the duct.

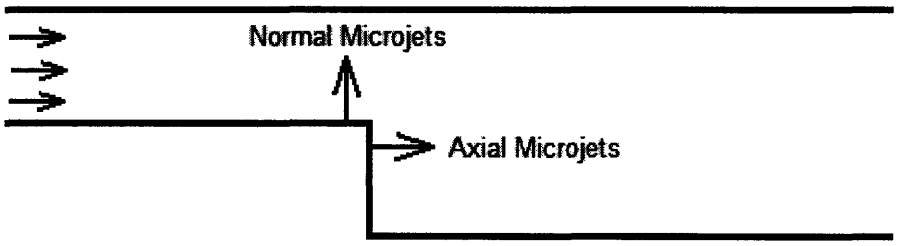

Figure 2-14: The relative position of the two microjet configurations seen from the side of the combustor with the fuel/air mixture entering from the left.

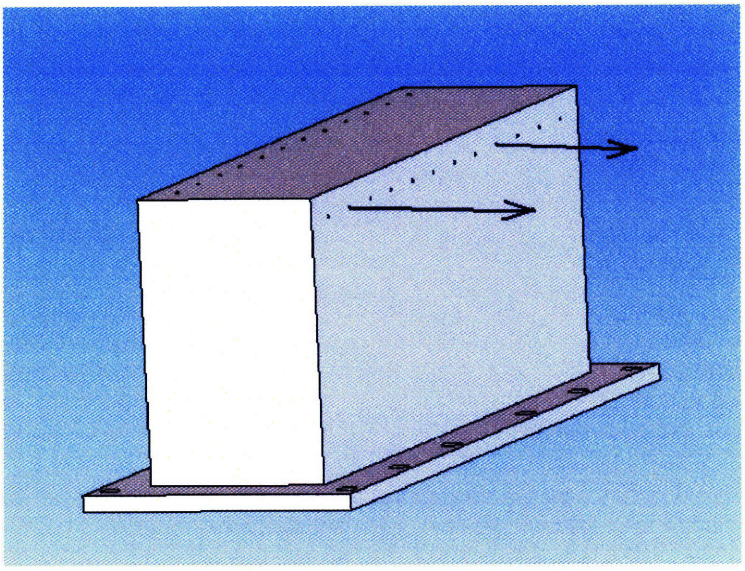

Figure 2-15: A schematic representation of the step manifold with the axial microjets location indicated. The top right edge closest to the arrows corresponds to the step corner in the combustor with the axial microjet configuration.

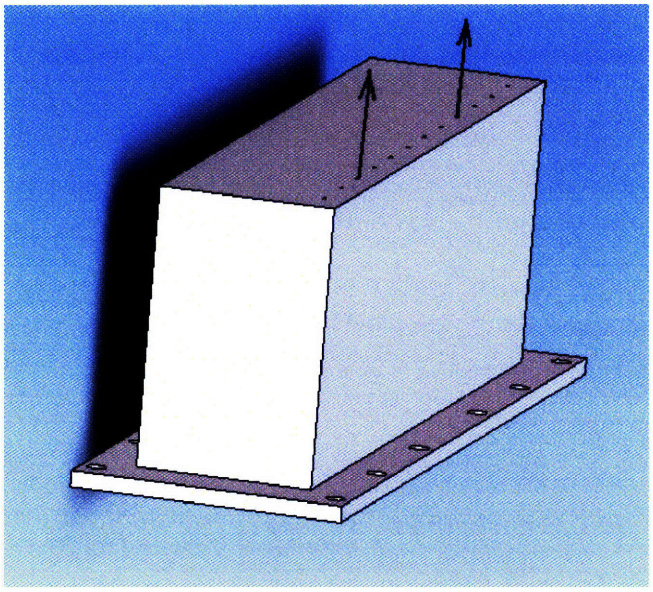

Figure 2-16: A picture of the step manifold with the normal microjets location indicated. The top right edge closest to the arrows corresponds to the step corner in the combustor with the axial microjet configuration.

Chapter 3

Results

Using the new diagnostic capabilities a substantial body of results was collected. Base assumptions about the inlet conditions were corroborated by first measuring them under nonreacting conditions. This included measuring the spatial equivalence ratio profile upstream of the combustion zone in order to observe the degree of premixedness. This spatial profile was also measured for both equivalence ratio and velocity downstream of the expansion to observe the impact of microjet air injection.

Under reacting conditions a wide parametric study was conducted to first determine under what conditions thermoacoustic instability is present, then to determine whether microjets could suppress these instabilities. Hysteresis effects were observed in the stability conditions. The impact of the fuel injection location was explored. It was found that the location of the fuel injection determined the strength of the coupling between equivalence ratio oscillations and acoustic oscillations. In exploring the conditions under which thermoacoustic instabilities were present, it was found that the combustion was unstable for equivalence ratios closer to the flashback limit. Thermoacoustic instabilities were not present for most cases when the equivalence ratio was close to the lean blowout limit when equivalence ratio oscillations were not present. When the fuel was injected 28 cm upstream of the expansion, coupling the

equivalence ratio to the acoustic oscillations, it was not possible to find conditions without thermoacoustic instabilities. By adding hydrogen to the fuel the lean blowout limit was lowered in all cases, but the transition to the unstable region would shift to lower equivalence ratios.

There were several dynamic states observed in the combustor that depended on the inlet conditions. These states varied in the frequency and intensity of the acoustic oscillations as well as the dynamic behavior of the flame front. The combustor acoustics were analyzed to determine the acoustic wave mode of the combustor at certain inlet conditions. The impact of both the normal and axial microjet air injection on the combustion dynamics was thoroughly explored. Several key conditions were recorded with peripheral diagnostics and high-speed video. Under conditions of pure propane the axial microjet injection was the most effective at widening the range of stability in the system.

3.1 Spatial ϕ

The spatial ϕ profile was measured at all cases with 300 K inlet air temperature and Re = 6500 in non-reacting flow. The profile was measured on a plane parallel to the front step face at a location 1 cm upstream of the expansion as shown in figure 3-1. The initial purpose for measuring the spatial distribution of the fuel concentration was to determine whether the fuel/air mixture entering the combustion zone was truly premixed. What I discovered was that the fuel was indeed premixed when the fuel was injected 93 cm upstream of the step as shown in figure 3-2. When the same fuel injector bars were used at the 28 cm location of the step there was a significant lack of uniformity in the concentration profile as shown in figure 3-3. It was determined that this fuel distribution was caused by the fact that a stagnation point is reached at the end of each of the fuel bars, which means that a stagnation pressure is present at

the end of each fuel bar. The presence of the this pressure gradient means that there will be a higher fuel flow rate out of the holes closer to the end of the fuel bar than there will farther away from the end. Since the fuel bars inject fuel from both side walls of the combustor, the result is the fuel distribution as shown in figure 3-3 where the concentration is greater in the middle of the duct than it is near its sides. This distribution defeats the purpose of the wide narrow duct design since the dynamics under these conditions can no longer be considered two-dimensional. This is also why the results from injecting the fuel at the 28 cm location in the previous combustor design were too dubious to be published.

The new fuel injector design provides a marked improvement on the distribution of the fuel close to the step as shown in the figure 3-4. Here the fuel distribution varies around %6 instead of the %10 variation with the holed fuel bars.

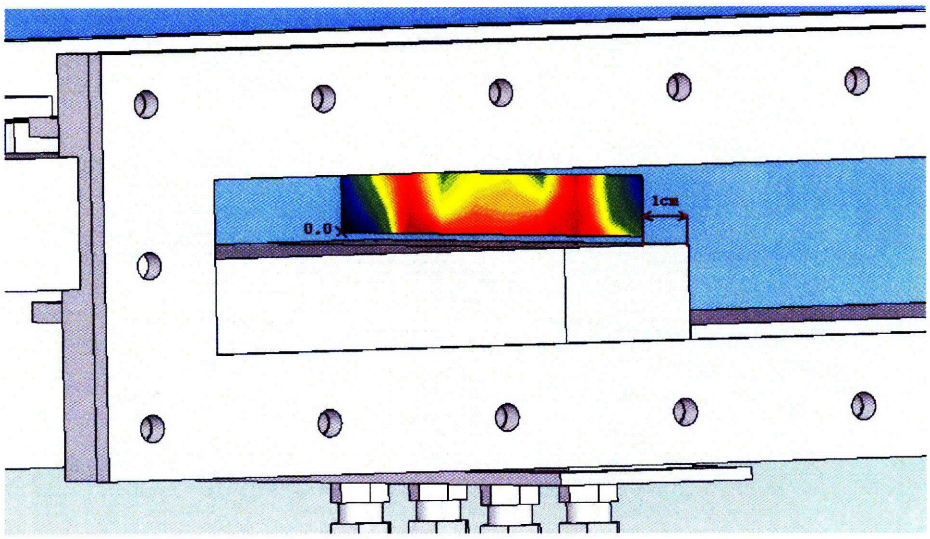

Figure 3-1: A schematic representation showing the position and orientation of the upstream spatial ϕ profile. The coordinates origin is marked and the plane is 1 cm upstream of the expansion and parallel to the front face of the step.

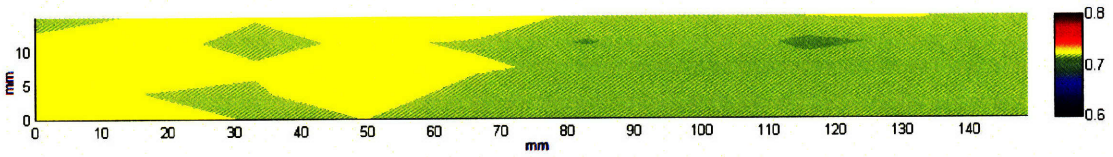

Figure 3-2: The spatial equivalence ratio profile for fuel injected 93 cm upstream of the step at $\phi = 0.7$, Re = 6500 and T_{in} = 300 K. The flow is non-reacting with holed fuel bar injection. The measurements are taken during nonreacting flow on a plane 1 cm upstream of the step as seen in figure 3-1.

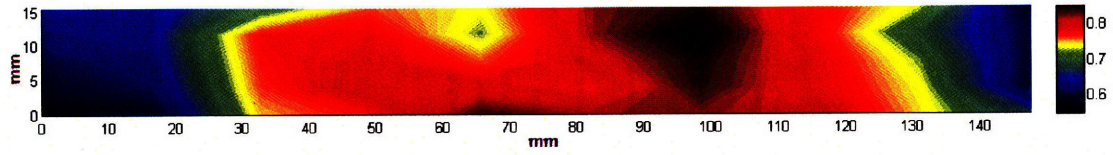

Figure 3-3: The spatial equivalence ratio profile for fuel injected 28 cm upstream of the step with fuel bars at $\phi = 0.7$, Re = 6500 and T_{in} = 300 K. The flow is non-reacting with holed fuel bar injection. The measurements are taken during nonreacting flow on a plane 1 cm upstream of the step as seen in figure 3-1.

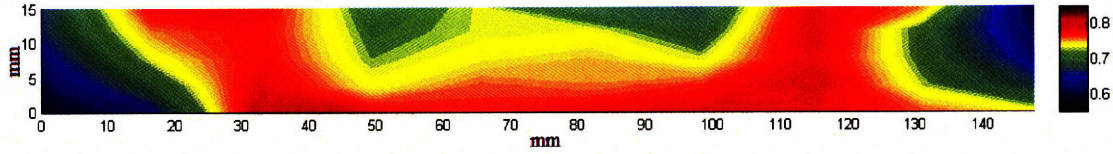

Figure 3-4: The spatial equivalence ratio profile for fuel injected 28 cm upstream of the step with microjet fuel injectors at $\phi = 0.7$, Re = 6500 and T_{in} = 300 K. The flow is non-reacting with new fuel injection manifold shown in figure 2-10. The measurements are taken during nonreacting flow on a plane 1 cm upstream of the step as seen in figure 3-1.

3.1.1 Effect of Microjets on Spatial ϕ

The ϕ profile as well as the $\overline{u}$ profile in section 3.2 were measured 2 cm downstream of the step as seen in figure 3-5. The plane does not extend closer to the top and bottom walls due to the limited range of the automated platforms, but the significant variations in the flow field occur in the middle of the duct where the shear layer is most prominent. Figure 3-6 shows the ϕ profile with 1 g/s of air injection through the normal microjets in non-reactive flow. It can be seen that there is a dilution of the overall equivalence ratio to around 0.61. There is a pocket of lower concentration mixture below the top surface of the step, which developed due to air being pulled in from the port slot of the gas probe and becomes trapped within the recirculation zone. Unfortunately this pocket of air is unavoidable for the experimental setup due to the fluid dynamics that are setup within this geometry. It is still clear from these results that at this plane of measurement there is no distinct distortion of the equivalence ratio profile due to the normal microjet injection.

Figure 3-7 shows the ϕ profile with axial microjet injection at 1 g/s of air. It can be seen that there is a localized dilution of the ϕ profile at the point of the microjet injection. This dilution could lower the flame speed directly in front of the jets, because it would be lowering the local equivalence ratio. Similar to the normal microjet case the added air reduces the average ϕ to a little over 0.61.

The dilution of the fuel due to the microjets is worth taking into account near the ranges of stability transitions where this shift in the equivalence ratio can make the difference between stable and quasi-stable dynamics. Keeping this in mind there is still the challenge of discriminating between the effect of this dilution and the natural hysteresis effects that are present in this combustor at these transition regions. The presence of hysteresis will be explored in more detail in section 3.3.

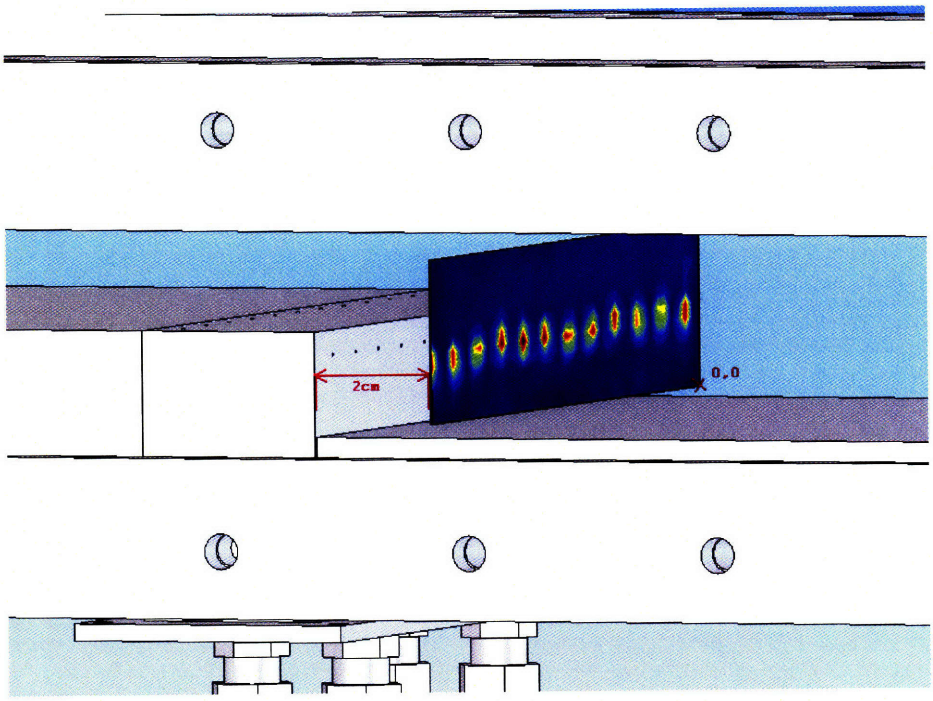

Figure 3-5: A schematic representation showing the position and orientation of the downstream spatial ϕ and $\overline{u}$ profile. The coordinates origin is marked and the plane is 2 cm downstream of the expansion and parallel to the front face of the step.

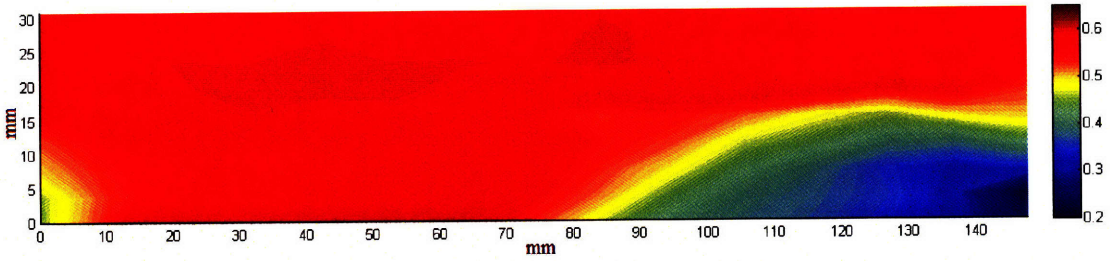

Figure 3-6: The spatial equivalence ratio profile for fuel injected 93 cm upstream of the step with normal microjets at $\phi = 0.65$, microjet flowrate of 1.0 g/s, Re = 6500 and T_{in} = 300 K. The measurements are taken during nonreacting flow on a plane 2 cm downstream of the step as seen in figure 3-5.

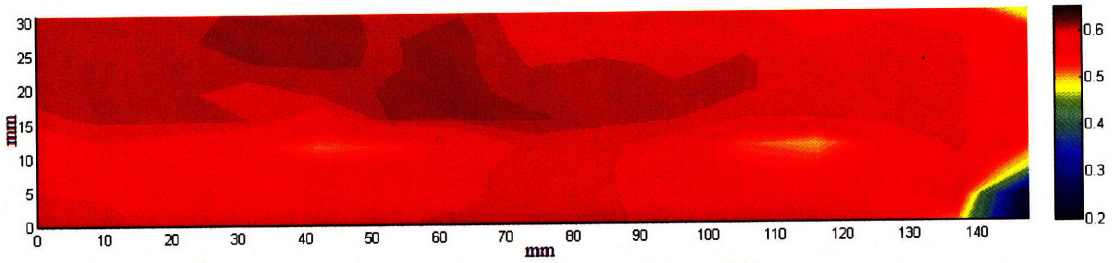

Figure 3-7: The spatial equivalence ratio profile for fuel injected 93 cm upstream of the step with axial microjets at $\phi = 0.65$, microjet flowrate of 1.0 g/s, Re = 6500 and T_{in} = 300 K. The measurements are taken during nonreacting flow on a plane 2 cm downstream of the step as seen in figure 3-5.

3.2 Spatial $\overline{u}$

Point measurements of the velocity magnitude were taken across a grid perpendicular to the flow located 2 cm downstream of the expansion at the location shown in figure 3-5. The data was taken during cold flow conditions. Figure 3-8 shows the velocity profile without microjets. The characteristic recirculation zone can be identified in the lower portion of the figure where the velocity is much lower. Due to the scale of the measurements the velocities in the recirculation zone are not easily identified. This condition coupled with the inability of the anemometer to indicate direction means that the hotwire anemometer is not an appropriate tool to measure the velocities within the steps recirculation zone. What is relevant from figure 52 is that downstream of the expansion there are three distinct velocity regions; a high velocity region above the top surface of the step, a low velocity region directly below the expansion and a high shear layer between the two.

Figure 3-9 shows the velocity profile with normal microjets at 1 g/s of air in a nonreacting flow. It can be seen that there is an increase in the spatial variation of the flow field. There is also an increase in the average measured velocity. This

profile shows that the normal microjets do have a substantial effect on the velocity profile entering the combustion region. Although from this measurement plane it is not possible to capture the full alteration of the flow field that is occurring directly within the vicinity of the normal microjets. This is not the case with the measurement of the axial microjets.

Figure 3-10 shows the velocity profile with axial microjets at 1 g/s of air in a nonreacting flow. At this plane the axial microjets dominate the flow field reaching a measured peak velocity of 25 m/s in front of each microjet. Comparing this profile to the equivalence ratio profile in figure 3-7, it appears that the axial microjets have a much greater impact on the velocity field than they do on the local fuel concentration.

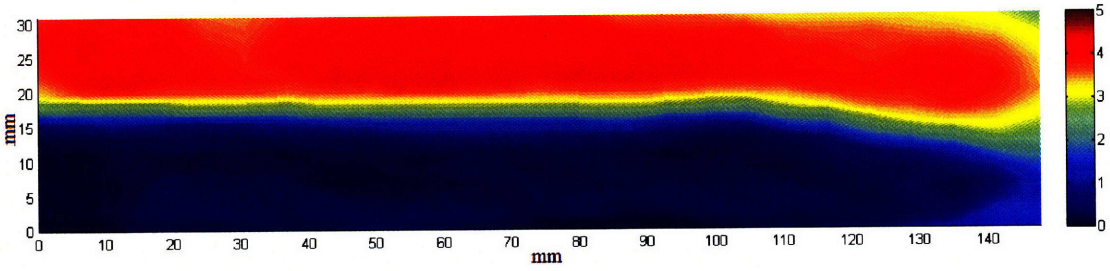

Figure 3-8: The velocity profile of the flow field 2 cm downstream of the step without microjets, Re = 8500 and T_{in} = 300 K. The measurements are taken during nonreacting flow on a plane 2 cm downstream of the step as seen in figure 3-5.

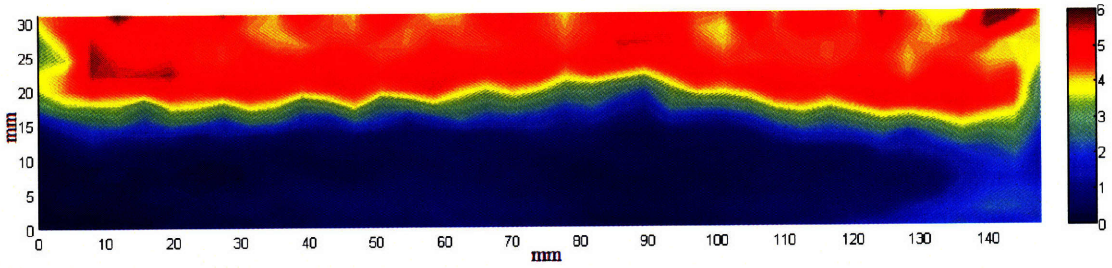

Figure 3-9: The velocity profile of the flow field 2 cm downstream of the step with a normal microjet flowrate of 1 g/s, Re = 8500 and T_{in} = 300 K. The measurements are taken during nonreacting flow on a plane 2 cm downstream of the step as seen in figure 3-5.

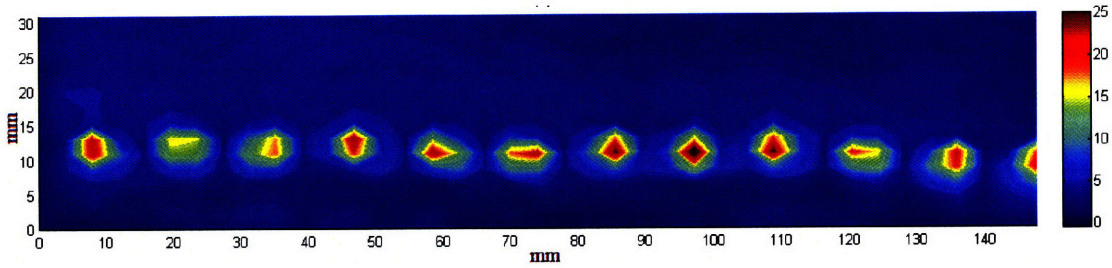

Figure 3-10: The velocity profile of the flow field 2 cm downstream of the step with a axial microjet flowrate of 1 g/s, Re = 8500 and T_{in} = 300 K. The measurements are taken during nonreacting flow on a plane 2 cm downstream of the step as seen in figure 3-5.

3.3 Hysteresis

Figure 3-11 shows the overall sound pressure level (OASPL) measured using the pressure sensor located 0.128 m downstream of the choke plate as a function of equivalence ratio at an inlet temperature of 300 K. This is without hydrogen enrichment and the fuel bar is located 93 cm upstream of the step for Reynolds numbers of 6500 and 8500. At each Reynolds number, the equivalence ratio is either increased from near the blowout limit towards stoichiometry, or decreased from near stoichiometry

towards the lean blowout limit. The OASPL in dB is defined as:

$$OASPL = 10\log_{10}\overline{\left[\frac{p(t)-\overline{p(t)}}{p_o}\right]^2} \tag{3.1}$$

where overbars indicate average values, $p(t)$ is the pressure measured in an interval $t_1 < t < t_2$ and $p_o = 2 \cdot 10^{-5}$ Pa. I observe that when I increase the equivalence ratio from the near the lean blowout limit, the transitions in the OASPL vs. ϕ data shown in figure 3-11 shift towards higher equivalence ratios at both Reynolds numbers. The dependence of combustor dynamics on the history, i.e. the presence of hysteresis, is attributed to the highly non-linear nature of the system. In the rest of the thesis all the data is obtained while decreasing the equivalence ratio from stoichiometry towards the lean blowout limit.

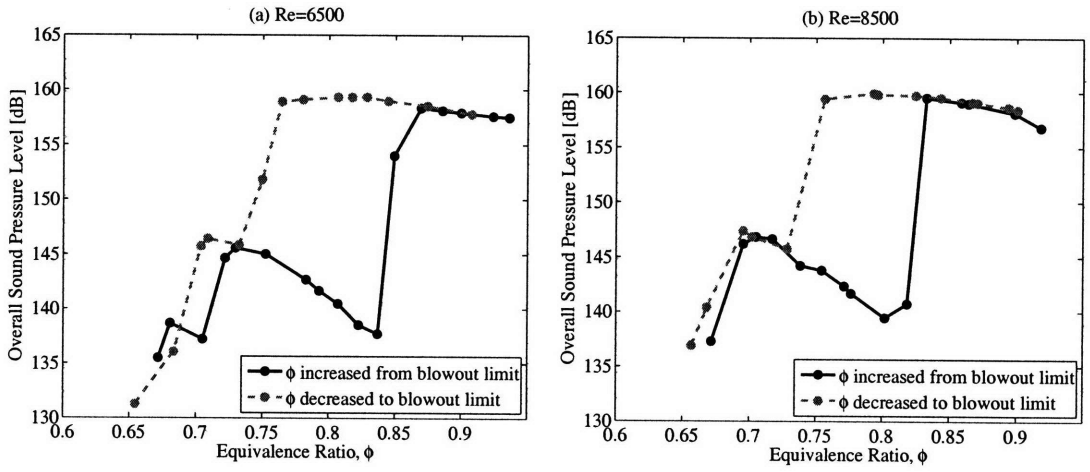

Figure 3-11: OASPL as a function of equivalence ratio without hydrogen enrichment when the fuel bar is located 93 cm upstream of the step at an inlet temperature of 300 K. The equivalence ratio is either increased from near the blowout limit towards stoichiometry, or decreased from near stoichiometry towards the lean blowout limit for: (a) Re=6500; (b) Re=8500.

3.4 Impact of Fuel Injection Location

I placed the fuel injector 28 cm or 93 cm upstream of the step to investigate the relative contributions of flame-vortex interactions and equivalence ratio oscillations on combustion dynamics. The temporal oscillations of the equivalence ratio, and the non-uniformity's in the equivalence ratio distribution entering the flame zone might significantly impact the combustion dynamics by impacting the flame structure. In order to achieve premixed combustion, the spatial equivalence ratio distribution entering the flame zone should be uniform. From section 3.1 I know that the fuel/air mixture is well mixed spatially with fuel injection 28 cm upstream of the step. I also know from the measurements shown that the mixture composition is more uniform when the fuel bar is located further from the step, as a result of the increased mixing time. In both locations of the fuel bar, the uniformity of the mixture composition is satisfactory, resulting in premixed combustion.

In figure 3-12 we show the temporal variation of the equivalence ratio measured 14 cm upstream of the step when the combustor is fired at an equivalence ratio of 0.80, Reynolds number of 8500, without hydrogen enrichment, for each location of the fuel bar. When the fuel is injected 93 cm upstream of the step, no temporal variations of the equivalence ratio are observed as a result of two factors: i) the amplitude of equivalence ratio oscillations established at the fuel bar are small since the fuel bar is located near the choke plate where velocity oscillations are small and ii) the convective time scale, $\tau = L/\bar{U}$ is long so that there is enough time for the oscillations to be damped by turbulent mixing before reaching the combustion zone, where L is the distance between the fuel injector and the step and $\bar{U}$ is the average flow velocity. In this case, the combustion dynamics are driven only by the flame-vortex interactions. When the fuel bar is placed 28 cm upstream of the step, significant temporal variations in the equivalence ratio are observed ranging from 0.45 to 1.3. The combustion dynamics are governed by both flame-vortex interactions and the

equivalence ratio oscillations. The equivalence ratio oscillations shown in figure 3-12(b) have a sharp peak and a blunt peak in each cycle. The blunt peak appears as a result of flow reversal during part of the cycle.

Figure 3-13 shows the OASPL measured using the pressure sensor 0.128 m downstream of the choke plate as a function of equivalence ratio without hydrogen enrichment. The fuel bar is located 93 cm and 28 cm upstream of the step for Reynolds number of 6500 and 8500 and inlet temperature of 300 K. When the fuel bar is located 93 cm upstream of the step, I observed distinct operating bands corresponding to sound pressure levels of 158-162 dB, 145-150 dB and 135-140 dB. The combustor operating modes corresponding to the 158-162 dB bands are referred as *unstable*, 140 dB-150 dB bands are referred as *quasi-stable* and 135-140 dB bands are referred as *stable*. When the fuel bar is moved to 28 cm upstream of the step, the quasi-stable and stable bands disappear at both Reynolds numbers and the equivalence ratio at blowout increases. The combustor operates in the *mixed unstable* mode. At Reynolds number of 6500; the equivalence ratio oscillations act to increase the OASPL. Reducing the equivalence ratio below 0.70 causes the flame to blowout before reaching the quasi-stable operating band observed when the fuel is injected 93 cm upstream of the step. This is caused by the fact that at some part of the cycle the instantaneous equivalence ratio is significantly lower than the lean flammability limit, so the flame will blow out before reaching the leaner average ϕ. At a Reynolds number of 8500; when the fuel is injected 28 cm upstream of the step, the equivalence ratio oscillations act to decrease (increase) the OASPL compared to the case when the fuel is injected 93 cm upstream of the step for $0.75 < \phi < 0.80$ ($0.69 < \phi < 0.75$). When the fuel is injected 28 cm upstream of the step, reducing the equivalence ratio below 0.69 causes the flame to blowout before reaching the stable operating band observed when the fuel is injected 93 cm upstream of the step.

These observations suggest that the primary mechanism governing the combustion

dynamics is the flame-vortex interactions, whereas the equivalence ratio oscillations have a secondary impact. The impact of equivalence ratio oscillations depend both on the Reynolds number and the equivalence ratio, since both effect the phase between the equivalence ratio and the pressure at the flame location [23]. In a backward-facing step combustor, the flame-vortex interactions are always present regardless of the fuel injection location. Therefore, it is important to develop reduced order models predicting the impact of flame-vortex interactions and it is misleading to include only the impact of equivalence ratio oscillations on combustion dynamics.

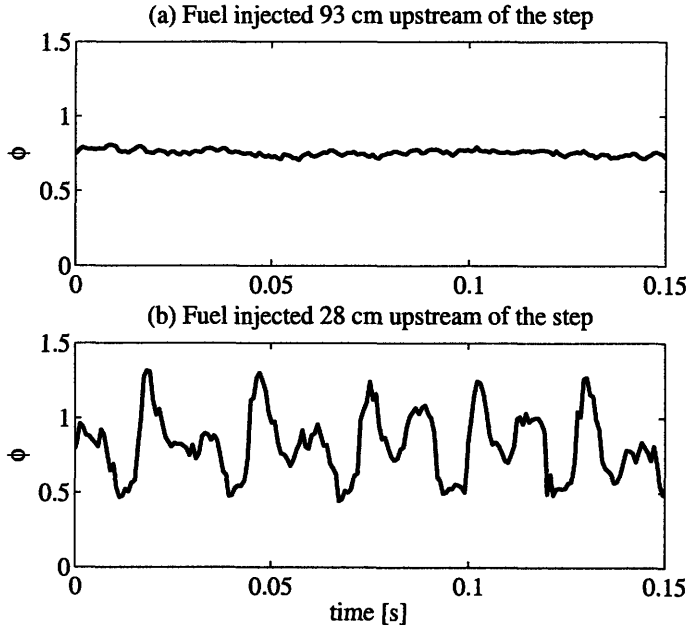

Figure 3-12: Temporal equivalence ratio measurements 14 cm upstream of the step at Re=8500, equivalence ratio set at 0.80. (a) Fuel injected 93 cm upstream of the step; (b) fuel injected 28 cm upstream of the step.

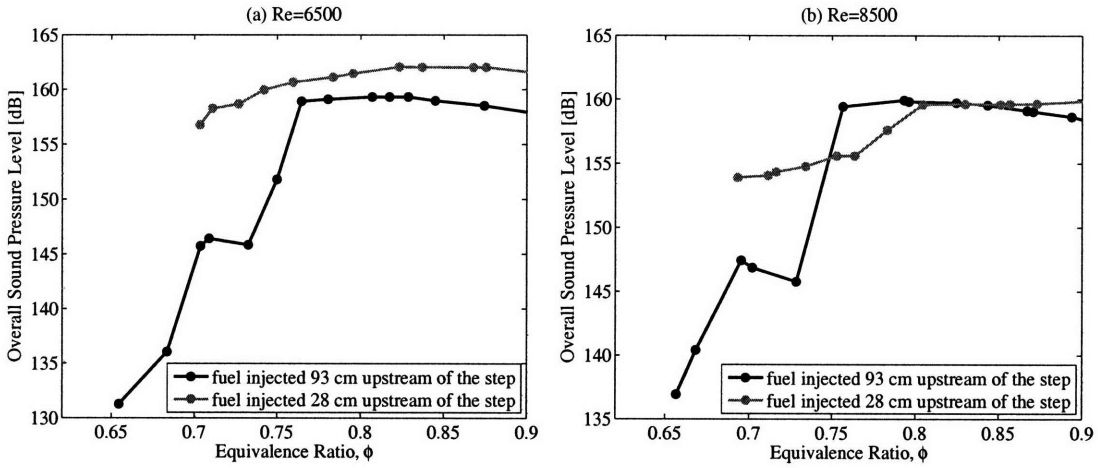

Figure 3-13: OASPL as a function of equivalence ratio without hydrogen enrichment when the fuel bar is located 93 cm or 28 cm upstream of the step at an inlet temperature of 300 K at (a) Re=6500; (b) Re=8500.

3.5 Stability Maps

I conducted a series of experiments in order to: i) determine the stability map; ii) understand the individual impacts of flame-vortex interactions and equivalence ratio oscillations. I fired the combustor at Reynolds numbers of 6500 and 8500 based on the step height using pure propane or propane enriched with hydrogen by adding 30% by volume (2% by mass; 4.8% by LHV) or 50% by volume (4.4% by mass; 10.6% by LHV) hydrogen. At each fuel composition and Reynolds number, I varied the equivalence ratio of the fuel-air mixture from near the lean blowout limit to a value approaching the flashback limit. I increased the inlet temperature up to 600 K for Reynolds number of 6500, and 500 K for Reynolds number of 8500. I conducted these experiments with the fuel bar located 93 cm upstream of the step and repeated several of them with the fuel bar 28 cm upstream of the step. Depending upon which fuel injection location I chose I was able to couple or decouple the flame-vortex-acoustic interactions from the equivalence ratio oscillations. The overall sound pressure level (OASPL) was

measured in the combustor for these varying parameters of the system. OASPL was used as the gauge for the level of intensity of the thermoacoustic instability.

3.5.1 Impact of H_2 Addition on Stability

Figure 3-14 shows the measured OASPL in dB for a range of ϕ and three different H_2concentrations at 0%, 30% and 50% H_2 by volume. With all three fuel compositions there is a narrow region at which the acoustic oscillations increase in intensity by at least 10 dB. The cases at the higher OASPL are considered unstable dynamics, whilst the cases with lower dB are considered either stable or quasi-stable. Each band of behavior has characteristic dynamics that make them distinct from each other beyond the OASPL. It can be observed in the figure 3-14 that the transition to the unstable case occurs at lower equivalence ratios as you increase the amount of H_2in the fuel. This coincides with the lowering of the lean blowout limit for the combustion, which is a predictable consequence of H_2 enrichment [28, 37, 38, 39]. The lowering of the lean blowout can be attributed to the increased differential diffusion effects caused by hydrogen enrichment, which increases the flame speed [40].

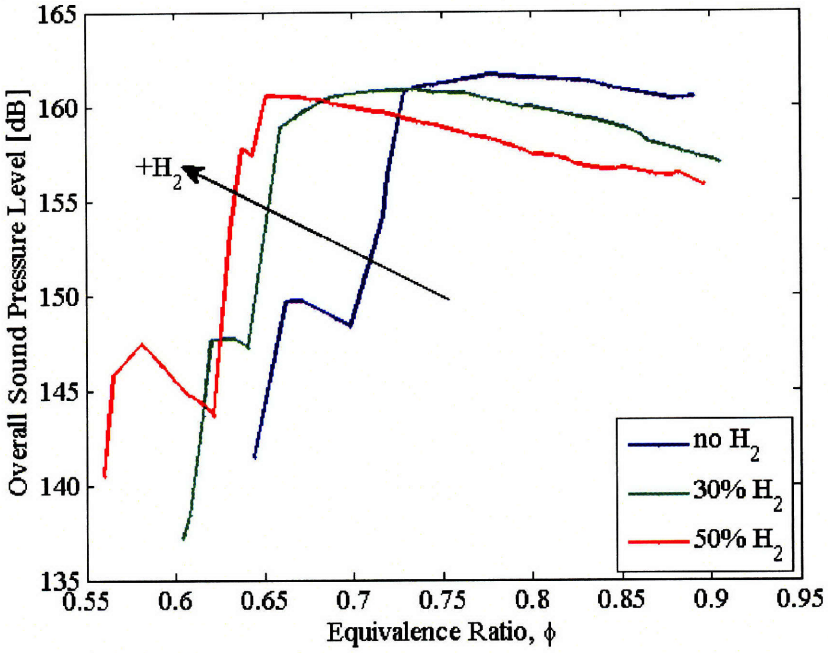

Figure 3-14: The stability map of a propane/hydrogen mixture for fuel concentrations at 0%, 30% and 50% H_2 by volume. The inlet air temperature is 300K and Re = 8500. The fuel was injected 93 cm upstream of the expansion.

3.5.2 Impact of Reynolds Number on Stability

In figure 3-15, the OASPL is plotted as a function of the equivalence ratio using pure propane or propane enriched with 50% by volume (4.4% by mass; 10.6% by LHV) hydrogen at Reynolds numbers of 6500 and 8500, and inlet temperatures of 300 K and 500 K. The impact of Reynolds number on the stability map is minor. The quasi-stable mode is wider when Reynolds number is 8500, especially at inlet temperature of 500 K. Enriching propane with hydrogen and increasing the temperature of the inlet mixture lowers the lean flammability limit and shifts the observed transitions from unstable mode to quasi-stable mode to lower equivalence ratios.

I show the combustor's frequency response in figures 3-16 and 3-17 for the cases corresponding to figure 3-15(a) and 3-15(b), respectively. These figures show the

amplitude of pressure oscillations at each frequency and equivalence ratio. High amplitudes correspond to darker regions.

Figure 3-16(a) shows the frequency response for Reynolds number of 6500, inlet temperature of 300 K, without hydrogen enrichment. As the equivalence ratio is dropped from 0.90 to 0.70, the acoustic mode around 40 Hz is excited and the combustor is operating in the unstable mode. As the equivalence ratio is reduced just below 0.70, there is a slight increase in the resonant frequency, which shows the transition to the quasi-stable operating mode. As the equivalence ratio is decreased further until the lean blowout limit, the resonant frequency drops slowly. Similar acoustic response is observed in figure 3-16(b), which shows the frequency response for Reynolds number of 8500, inlet temperature of 300 K, without hydrogen enrichment. However, at this Reynolds number, the transition to the quasi-stable mode occurs around the equivalence ratio of 0.73, which is slightly higher than the Re=6500 case. When 50% by volume hydrogen is added to propane, the transition to the quasi-stable mode occurs at an equivalence ratio of 0.62 at both Reynolds numbers as shown in figures 3-16(c) and (d). When the inlet temperature is 300 K, only the lowest acoustic mode is dominant for the unstable and the quasi-stable operating modes of the combustor.

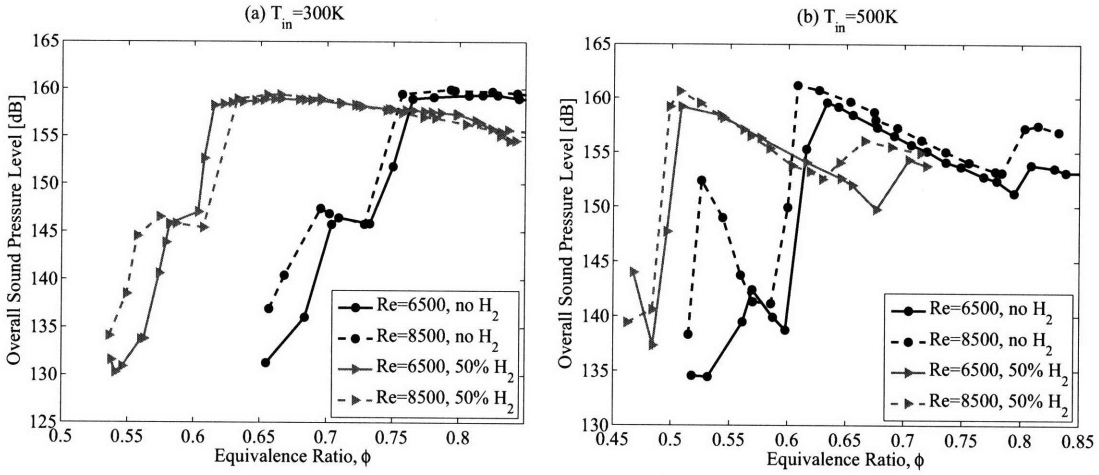

Figure 3-15: OASPL as a function of equivalence ratio using pure propane and propane enriched with 50% by volume hydrogen at Re=6500 and Re=8500 at an inlet temperature of (a) T_{in}=300 K; (b) T_{in}=500 K. The fuel is injected 93 cm upstream of the step.

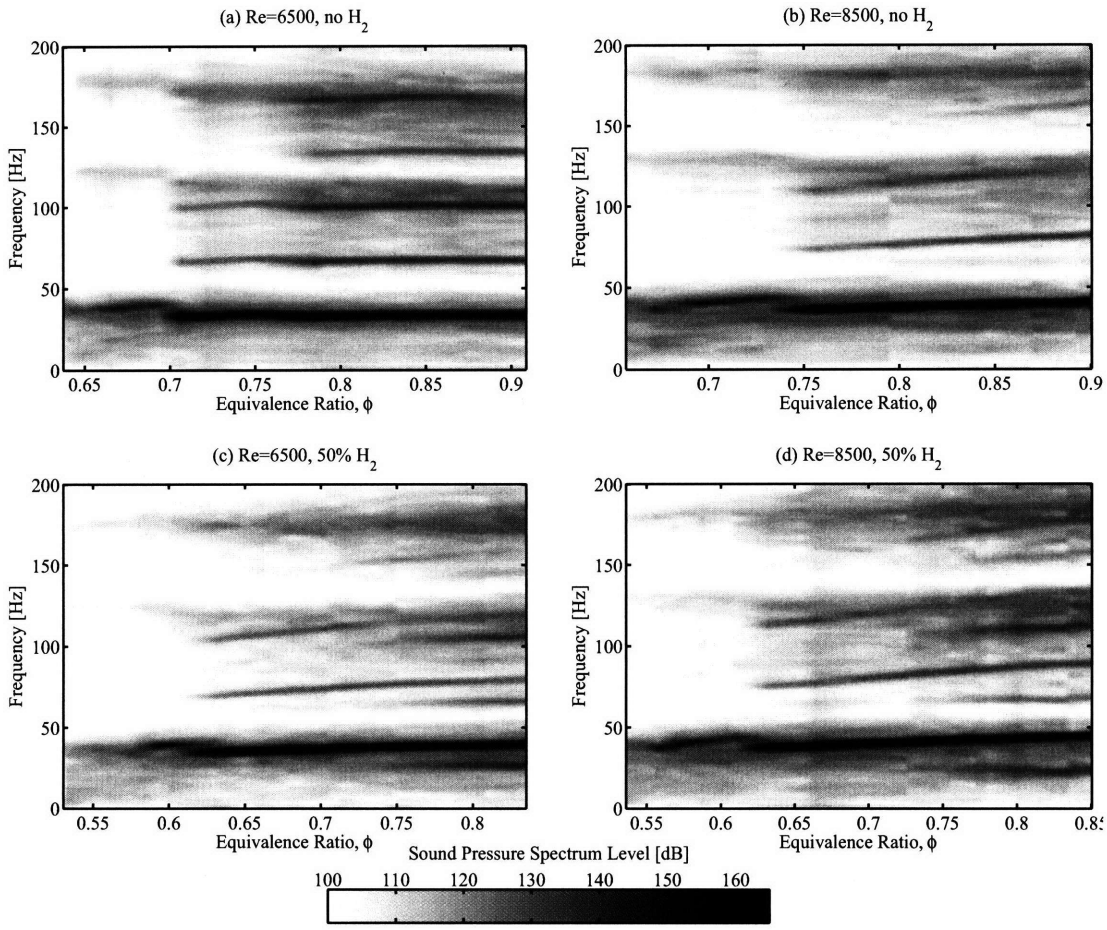

Figure 3-16: Sound pressure spectrum level maps as a function of equivalence ratio at inlet temperature of 300 K for (a) Re=6500, no H_2 enrichment; (b) Re=8500, no H_2 enrichment; (c) Re=6500, 50% by volume H_2 enrichment; (d) Re=8500, 50% by volume H_2 enrichment. Dark bands indicate high amplitude frequency components. The fuel is injected 93 cm upstream of the step.

3.5.3 Impact of Inlet Temperature on Stability

When the inlet temperature is increased to 500 K, there are significant changes in the acoustic response of the combustor as shown in figure 3-17. Without hydrogen addition, as the equivalence ratio is dropped from 0.85, the combustor resonates around 130 Hz until the equivalence ratio becomes 0.80 at both Reynolds numbers

as shown in figures 3-17(a) and (b). The operating bands correspond to 153 dB and 158 dB OASPL for Reynolds numbers of 6500 and 8500, respectively in figure 3-15(b), and referred to as the *high frequency unstable* mode. As the equivalence ratio is reduced further the 40 Hz band is excited until blowout. However, near the equivalence ratio of 0.60, at both Reynolds numbers the OASPL drops significantly, which shows the transition from unstable to quasi-stable band. The OASPL increases until the equivalence ratio is dropped to 0.57 and 0.52 for Reynolds numbers of 6500 and 8500, respectively. When 50% by volume hydrogen is added to propane, as the equivalence ratio is reduced from 0.72, the combustor resonates at 130 Hz until the OASPL reaches its local minimum around equivalence ratios of 0.68 and 0.65 for Reynolds numbers of 6500 and 8500, respectively, as observed in figure 3-15(b). As the equivalence ratio is reduced further, the 40 Hz band is excited until the combustor shifts from unstable to quasi-stable operating mode around equivalence ratio of 0.49 at both Reynolds numbers.

So far I observe that increasing the hydrogen content in the fuel and the inlet temperature effects the stability map of the combustor and the observed resonant frequencies significantly compared to the impact of changing the Reynolds number. I investigate the impact of hydrogen enrichment and the inlet temperature by extending the parameter set in figure 3-18 where I plot the OASPL as a function of the equivalence ratio at a Reynolds number of 6500 for different fuel compositions and inlet temperature. Figure 3-18 shows that at all inlet temperatures, increasing the amount of hydrogen in the fuel shifts the curves towards leaner equivalence ratios. This is because of the increased flame speed as a result of the high diffusivity of hydrogen. The distinct quasi-stable band disappears when the inlet temperature is 600 K. With preheating, the OASPL drops as the equivalence ratio increases until the higher frequency mode of the combustor is excited as shown in figure 3-18(c) and (d). At the local minimum, which is the transition point between unstable and high frequency

unstable modes, the combustor operates in the quasi-stable mode. Preheating the inlet mixture allows the excitation of higher frequency modes and increases the flame speed, impacting both the acoustic response and combustion dynamics significantly.

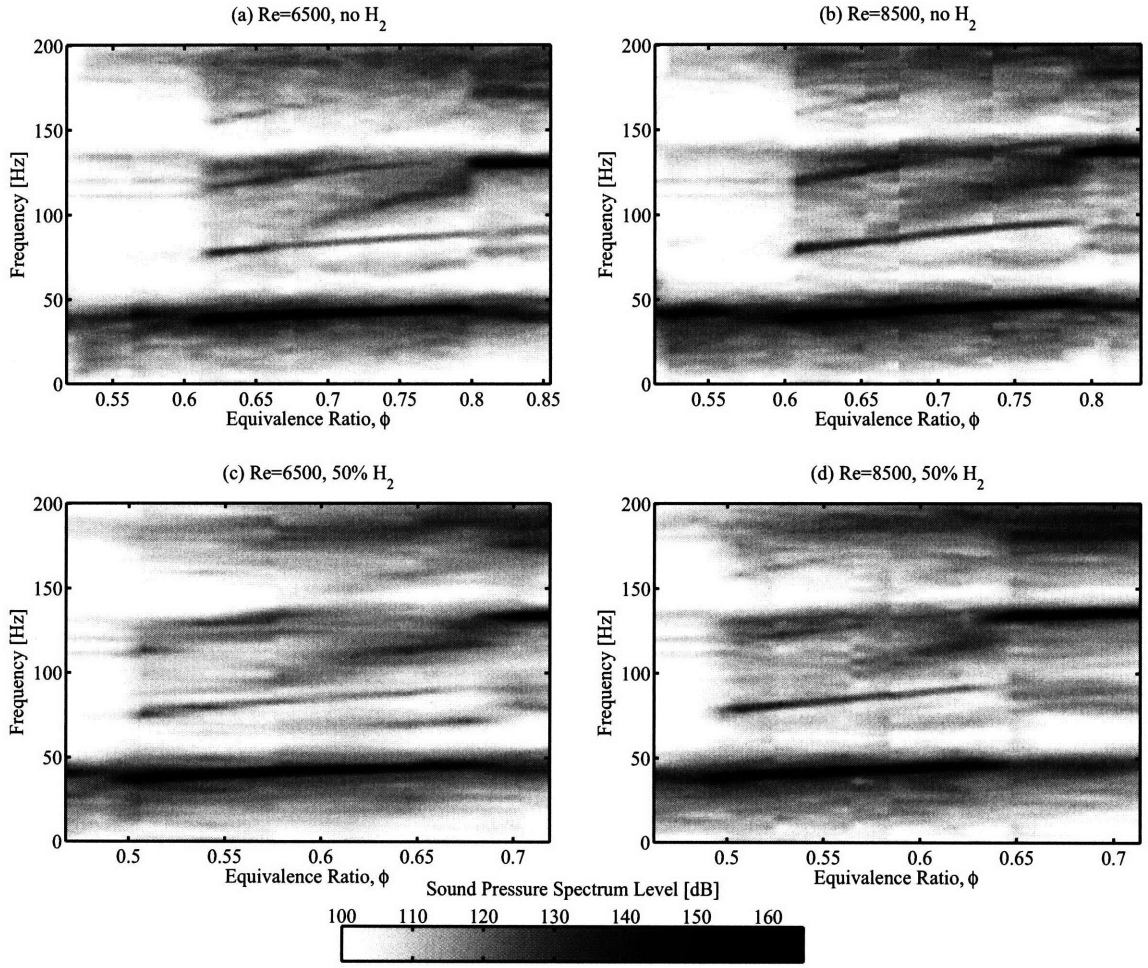

Figure 3-17: Sound pressure spectrum level maps as a function of equivalence ratio at inlet temperature of 500 K for (a) Re=6500, no H_2 enrichment; (b) Re=8500, no H_2 enrichment; (c) Re=6500, 50% by volume H_2 enrichment; (d) Re=8500, 50% by volume H_2 enrichment. Dark bands indicate high amplitude frequency components. The fuel is injected 93 cm upstream of the step.

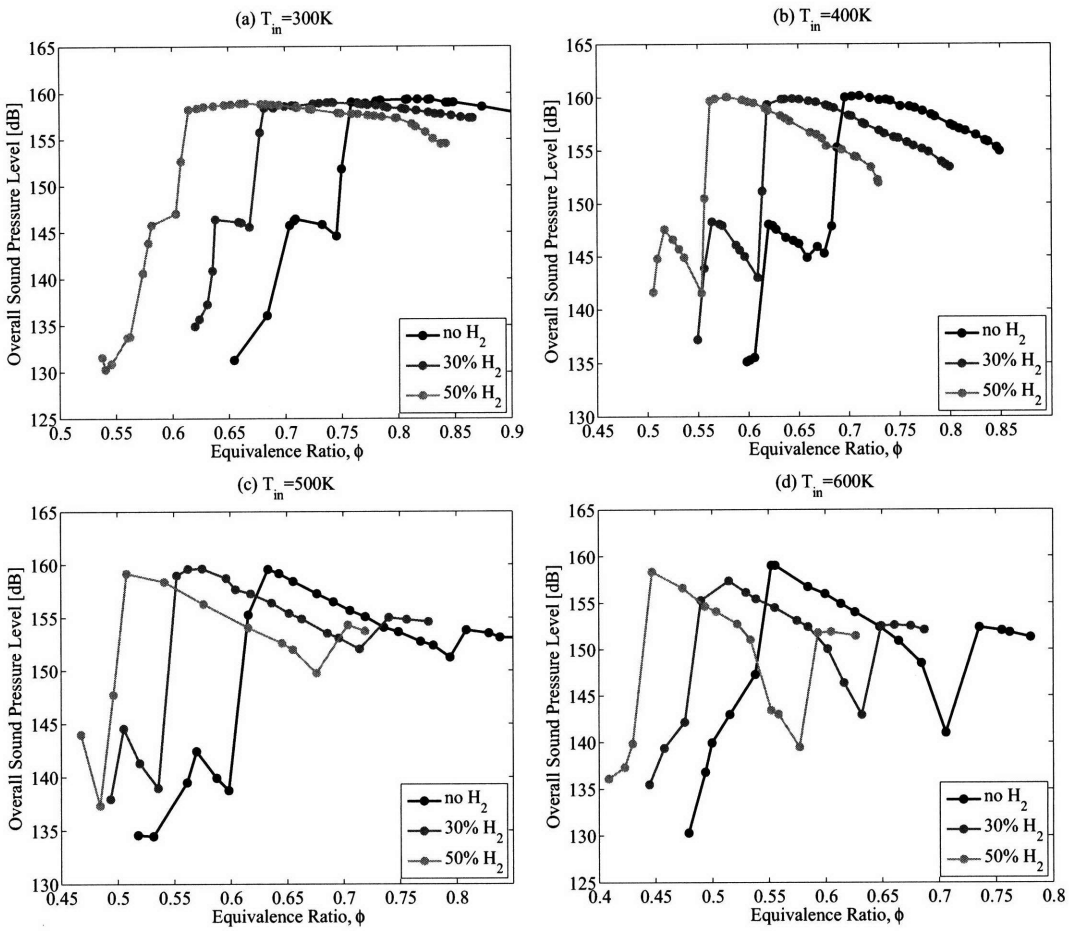

Figure 3-18: OASPL as a function of equivalence ratio at different hydrogen concentrations with (a) T_{in}=300 K; (b) T_{in}=400 K; (c) T_{in}=500 K; (d) T_{in}=600 K. Re=6500. The fuel is injected 93 cm upstream of the step.

3.6 Combustion Dynamics

I investigate flame images extracted from high speed videos of typical unstable, mixed unstable, high frequency unstable, quasi-stable and stable operating modes. This is supported by corresponding unsteady pressure (measured 0.128 m downstream of the choke plate), velocity, heat release rate and equivalence ratio measurements. The velocity is measured by inserting the hotwire anemometer 0.76 m downstream of the choke plate, which places it roughly 5-15 cm upstream of the flame depending on the

dynamics. This is close enough for a reasonable measurement of the velocity at the flame front, but far enough away that the flame will not damage the probe.

3.6.1 Velocity Reversal Compensation

A disadvantage of the hotwire anemometer is that it can only measure the *magnitude* of the velocity and not the direction. This means that if the flow in the combustor was reversed for part of the cycle, then the velocity would still be measured as positive. In the initial measurements of velocity it was observed that as the signal got close to 0 m/s it reversed itself quickly to make a small peak before reversing again and reverting to the dominant harmonic. This behavior is shown in figure 3-19. It was suspected that the flow was actually reversing and being recorded as positive, because the smaller peak was not being reflected in the pressure signal. It is reasonable to assume that the velocity would not go to absolute zero, because small scale turbulence in the flow will keep the sensor from seeing any instant of still flow. In order to thoroughly test whether the flow was reversing I decided to turn my attention to the ϕ signal corresponding to the velocity signal seen in the same figure 3-19. There appear to be two comparable harmonics in this data as well, but there is only a single dominant one in the pressure signal. I assumed that the higher frequency harmonic of ϕ was due to the flow reversal and simulated it numerically.

The numerical simulation consisted a one-dimensional diffusion model of air flow in a duct with propane being injected. There was a sinusoidal forcing velocity with peaks between -1.0-10 m/s whilst the injection flowrate of the fuel was kept constant. The results of this simulation are shown in figure 3-20, where the simulated equivalence ratio is recorded at a *fixed* point 1 cm downstream of the injection site. It can be seen that the velocity is negative for a small portion of its cycle. The temporal equivalence ratio shows the same double harmonic characteristics as those seen in figure 3-12(b). With this confirmation I decided to process the small peaks near 0 m/s as negative

velocities when the phenomenon occurred.

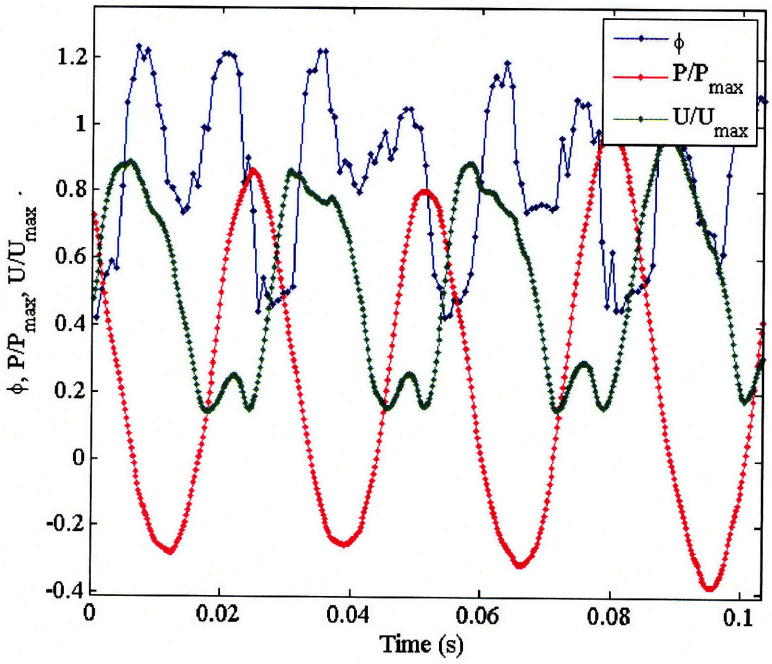

Figure 3-19: The simultaneous velocity, pressure and equivalence ratio signal at Re = 8500, $\phi = 0.85$, $T_{in} = 300$ K, and the fuel was injected 28 cm upstream of the step with micro-holed fuel injectors. The normalized velocity has *not* been corrected for backwards flow.

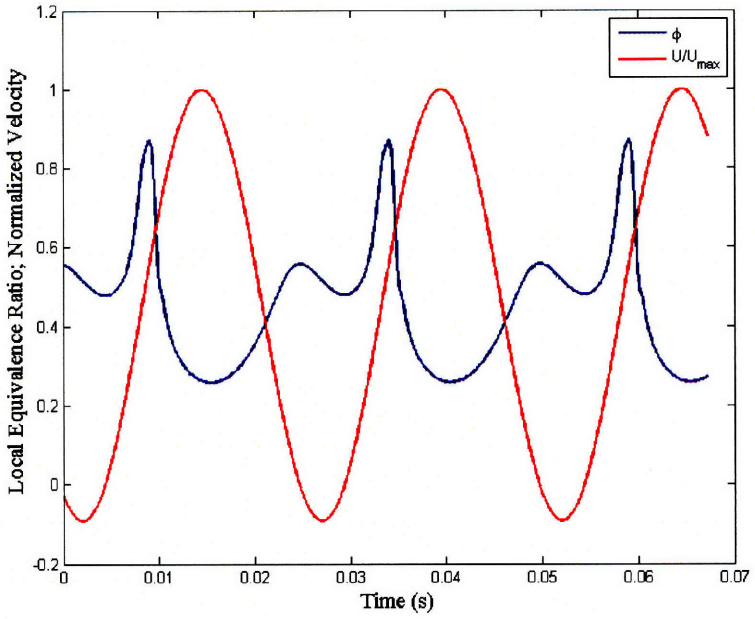

Figure 3-20: A one-dimensional numerical simulation of propane injected into a flowing duct to simulate the effect of flow reversal on the temporal variation of equivalence ratio. The inlet equivalence ratio is ϕ =0.57 with a sinusoidal forcing velocity with peaks between -1.0-10 m/s. The simulated equivalence ratio is measured at a fixed point 1 cm downstream of the fuel injection site.

3.6.2 Unstable Mode

In figure 3-21, I show a sequence of flame images corresponding to the unstable mode observed when the fuel bar is located 93 cm upstream of the step; ϕ=0.80, Re=8500, T_{in}=300 K, without hydrogen enrichment. Figure 3-22 shows simultaneous heat release rate, velocity, pressure and equivalence ratio measurements corresponding to the instances shown in figure 3-21. The resonant frequency is 36 Hz, which corresponds to the quarter wave mode of the combustor. In the unstable mode, a wake vortex is formed from the recirculation zone downstream of the step (1). At this moment the velocity increases near maximum acceleration and pressure is at its maximum. As

the inlet velocity increases, the vortex convects downstream and grows in size and as a result a pocket of unburned reactants is formed (2, 3). In addition, the heat release rate drops as the intense burning taking place from the previous cycle near the upper wall of the combustor is completed. Between instances 2 and 3, heat release rate reaches its minimum, whereas the velocity is near its maximum value. As the velocity drops from its maximum value, the vortex continues to move downstream and grows towards the upper wall of the combustor. The heat release rate starts rising as burning of the reactant pocket initiates (4-6). When the velocity becomes minimum between images 6 and 7, the vortex reaches the upper wall of the combustor, which collapses the reactant pocket, causing intense burning. As a result, the heat release rate reaches its maximum corresponding closely to the moment of maximum pressure, resulting in the positive feedback between the unsteady heat release rate and the pressure, which feeds the instability (7). The flame moves upstream of the step as a result of the negative inlet velocity (7, 8). As the inlet velocity increases, heat release rate starts to drop, fresh reactants enter the flame anchoring zone and the cycle repeats. Since the fuel bar is located far enough from the combustion zone, the equivalence ratio remains nearly constant throughout the cycle. Therefore, the instability is purely driven by the flame-vortex interactions.

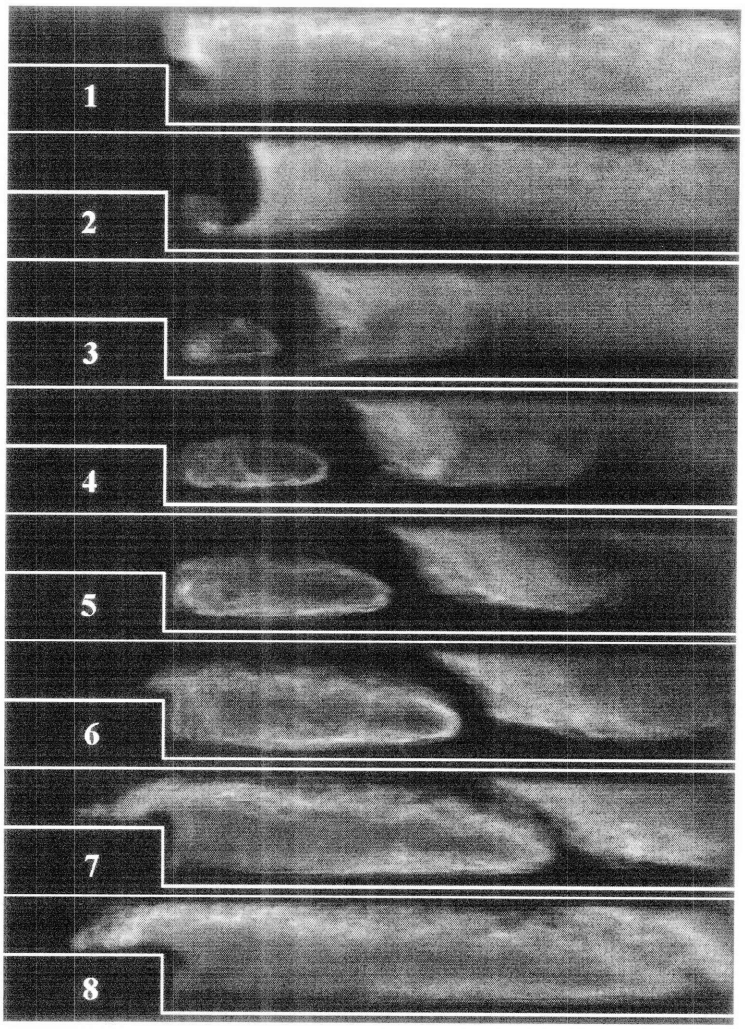

Figure 3-21: Flame images of unstable mode without hydrogen enrichment when the fuel bar is located 93 cm upstream of the step. ϕ=0.80, Re=8500, T_{in}=300 K. The resonant frequency is 36 Hz. The time between frames is 4 ms.

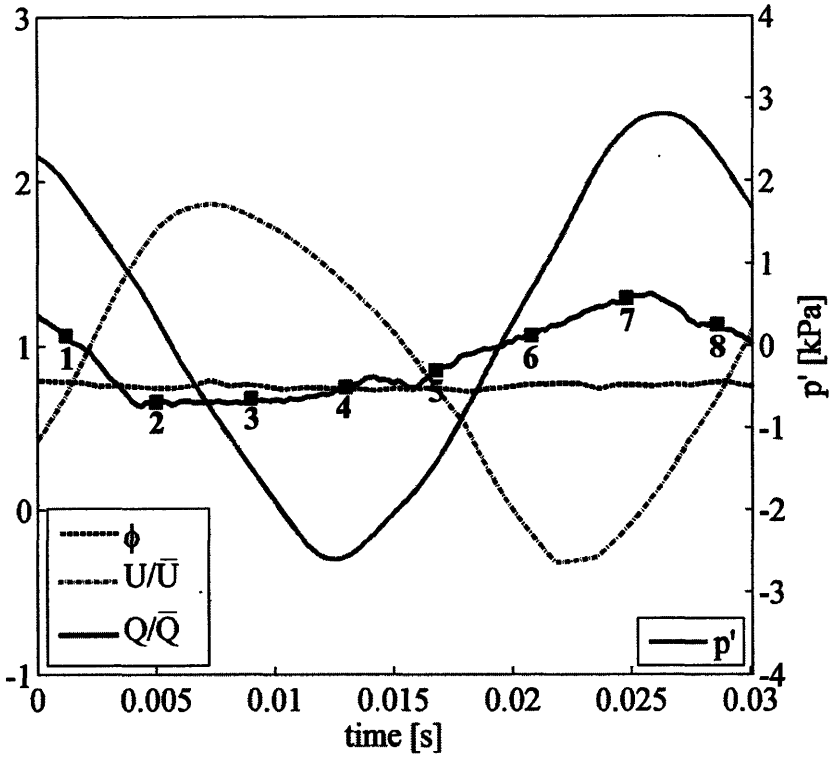

Figure 3-22: Simultaneous heat release rate, velocity, pressure and equivalence ratio measurements corresponding to the unstable mode shown in figure 3-21.

3.6.3 Mixed Unstable Mode

In figure 3-23 a sequence of flame images is shown corresponding to the mixed unstable mode observed when the fuel bar is 28 cm upstream of the step, using the same parameters while describing the unstable mode; ϕ=0.80, Re=8500, T_{in}=300 K, without hydrogen enrichment. Figure 3-24 shows simultaneous heat release rate, velocity, pressure and equivalence ratio measurements corresponding to the instances shown in figure 3-23. As mentioned before, at this location of the fuel bar, equivalence ratio entering the combustion zone oscillates. I perform the equivalence ratio measurements 14 cm upstream of the step. In order to accurately determine the equivalence ratio entering the combustion zone, I phase-shifted the measured equivalence ratio

with the convective time scale $\tau = L_m/\bar{U}$, where L_m is the distance between the step and the location of the ϕ measurement (14 cm), and $\bar{U}$ is the mean velocity (6 m/s). The equivalence ratio measurements shown in figure 3-24 reflects this phase shift. The resonant frequency is 35 Hz, which corresponds to the quarter wave mode of the combustor.

As shown in figure 3-24, at instance 1, the heat release rate is dropping as the intense burning taking place from the previous cycle is completed. Near the moment of maximum acceleration a wake vortex is shed from the recirculation zone downstream of the step and convects downstream (2-4). At instances 2 and 3, the equivalence ratio entering the step is at its minimum around 0.50, causing the flame to nearly blowout. This explains the lack of intensity in images 2 and 3 in figure 3-23. Unlike the previous case when the instability is driven solely by flame-vortex interactions, I do not observe sudden burning of a reactant pocket. Intense burning initiates near the lower wall of the combustor as the equivalence ratio reaches its maximum around 1.2 (4). As the vortex moves downstream and grows in size while the inlet velocity drops, burning continues and the heat release rate rises (5, 6), reaching its maximum value near instance 6. At this instance the velocity is at its minimum value. Heat release rate drops quickly as the velocity recovers (7, 8). The flame moves slightly upstream of the step only at instance 7. The cycle repeats as the fresh mixture is admitted into the flame anchoring zone (1). The pressure oscillations lag the heat release rate by approximately 70 degrees, resulting in positive feedback between heat release rate and pressure. Although the heat release rate oscillations are stronger in this case compared to the unstable mode, the resulting OASPL is lower as shown in figure 3-13(b). This is because of the higher phase between heat release rate and pressure, i.e. weaker positive feedback. Since the equivalence ratio is significantly higher than its average value as the intense burning initiates, the heat release rate reaches its maximum value quicker compared to the unstable mode, which causes the

higher phase between heat release rate and pressure oscillations.

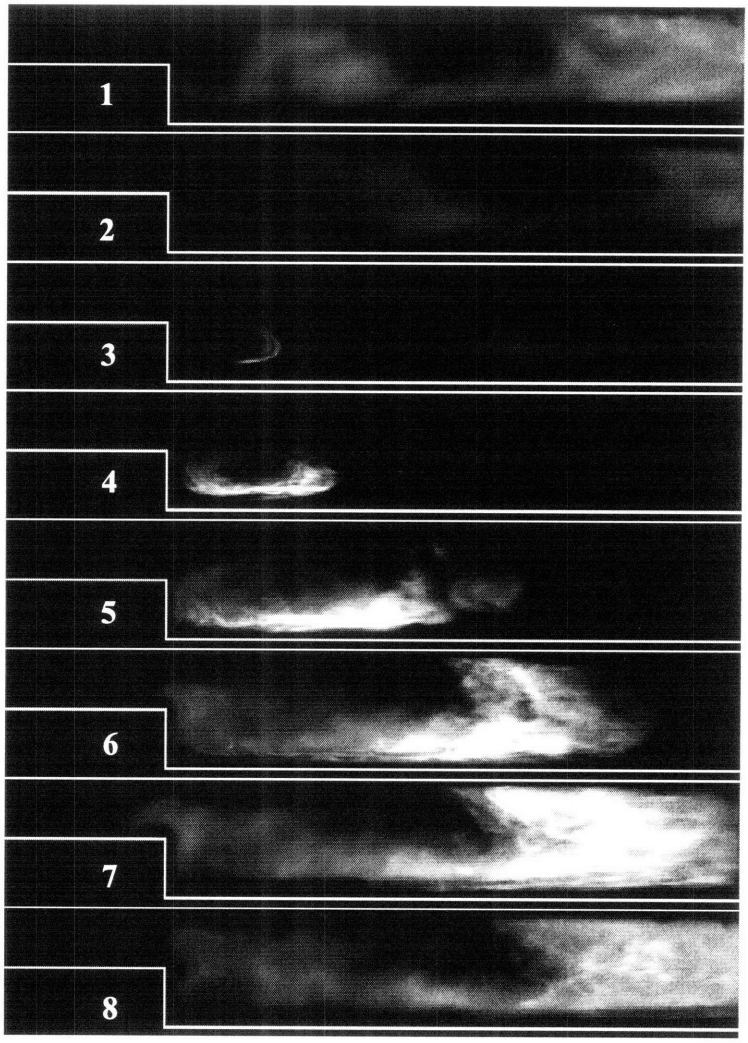

Figure 3-23: Flame images of mixed unstable mode without hydrogen enrichment when the fuel bar is located 28 cm upstream of the step. ϕ=0.80, Re=8500, T_{in}=300 K. The resonant frequency is 35 Hz. The time between frames is 4.1 ms.

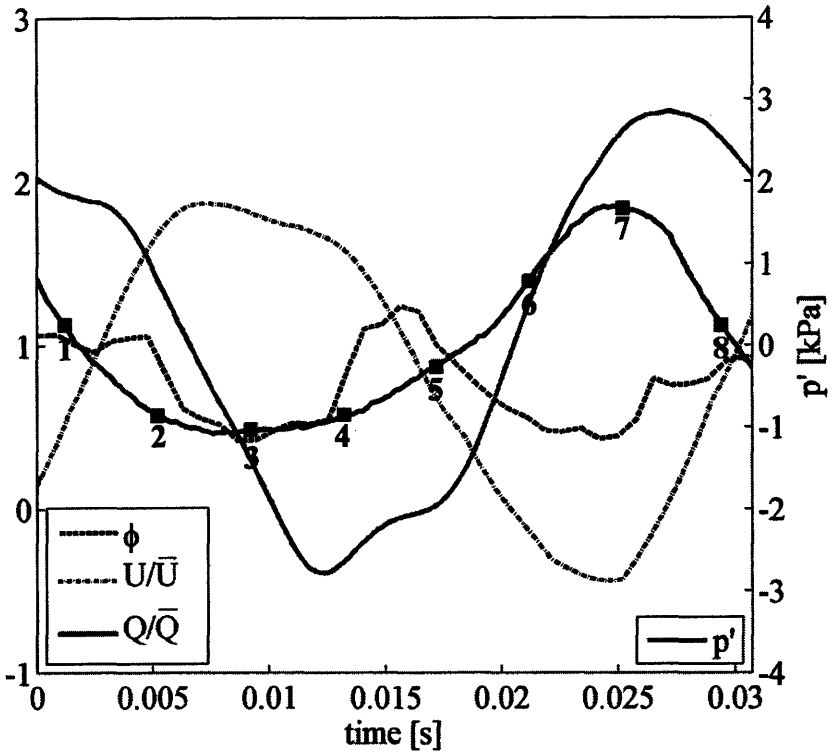

Figure 3-24: Simultaneous heat release rate, velocity, pressure and equivalence ratio measurements corresponding to the mixed unstable mode shown in figure 3-23.

3.6.4 High Frequency Unstable Mode

When the inlet mixture is preheated to higher temperatures, I observe instability at higher frequencies. Figure 3-25 shows a sequence of flame images corresponding to the unstable mode observed when the fuel bar is located 93 cm upstream of the step; $\phi = 0.70$, Re = 6500, $T_{in} = 500$ K and the propane is enriched with 50% by volume hydrogen. Figure 3-26 shows simultaneous heat release rate and pressure measurements corresponding to the instances shown in figure 3-25. Point velocity measurements were not done for this case, because the hot wire anemometer would need to be recalibrated for the higher temperature. The recalibration would need to account for minor fluctuations in the temperature due to imperfect preheating

control. Finding a solution to this recalibration problem is beyond the scope of this work and therefore only measurements at $T_{in} = 300$ K were taken.

The equivalence ratio is constant since the fuel bar is located far from the step. The resonant frequency is 132 Hz, which corresponds to 3/4 wavemode of the combustor. The observed combustion dynamics is very similar to the unstable mode, except that the unsteady flame dynamics is faster in this case. As a result of the higher frequency, the flame is more compact and the wake vortex reaches the upper wall of the combustor closer to the step. The heat release rate and pressure oscillations are in-phase, resulting in the observed instability. More compact flame causes smaller variation in the flame surface area, resulting in smaller amplitude heat release rate oscillations compared to the unstable case. The unsteady pressure amplitude is also lower than the unstable case as a result of the smaller energy supplied to the acoustic mode due to heat release.

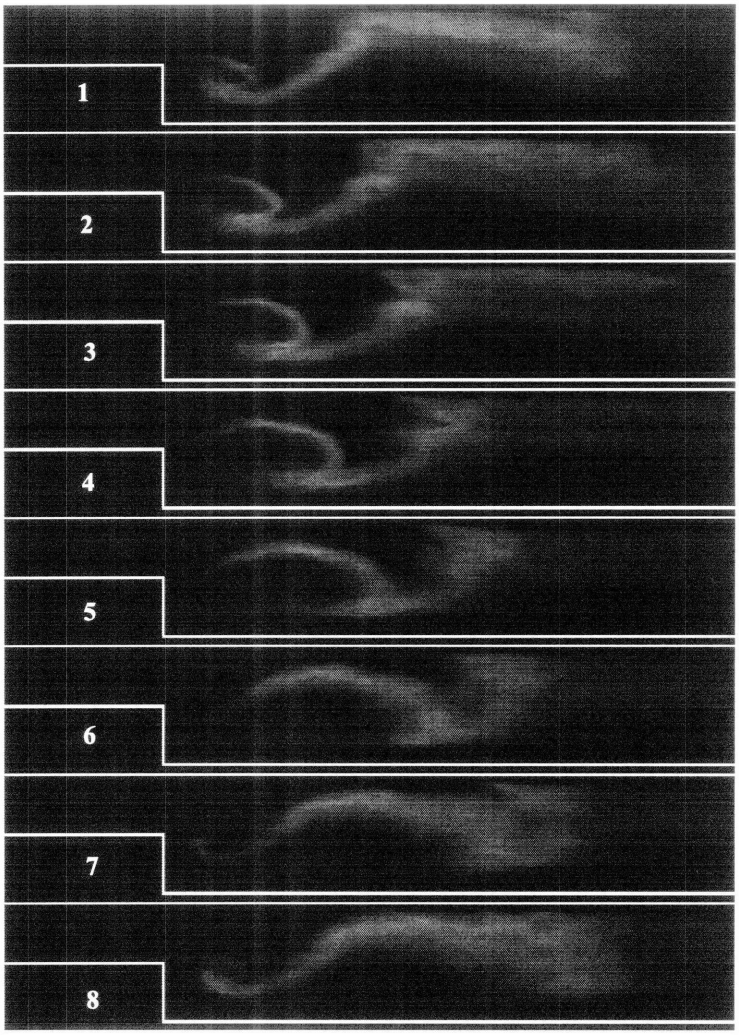

Figure 3-25: Flame images of high frequency unstable mode with 50% by volume hydrogen enrichment when the fuel bar is located 93 cm upstream of the step. ϕ=0.70, Re=6500, T_{in}=500 K. The resonant frequency is 132 Hz. The time between frames is 1.1 ms.

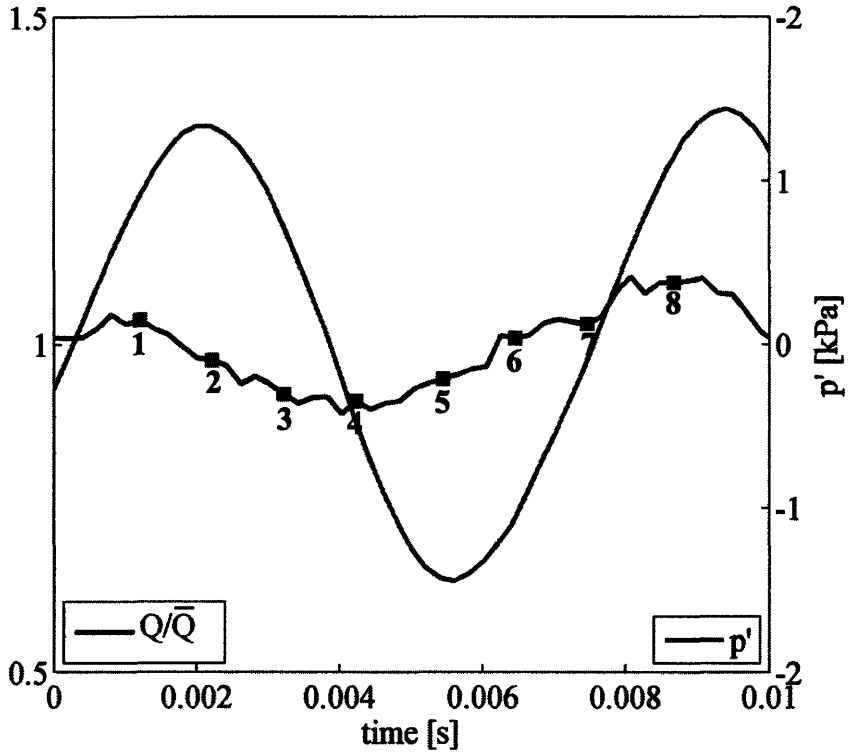

Figure 3-26: Simultaneous heat release rate and pressure measurements corresponding to the high frequency unstable mode shown in figure 3-25.

3.6.5 Quasi-stable Mode

When the equivalence ratio is dropped while the combustor is operating in the unstable mode, the noise from the combustor drops significantly when the equivalence ratio is lower than a certain value depending on the operating conditions. This is the quasi-stable operating mode of the combustor which corresponds to the 140 dB-150 dB plateau observed in figure 3-18. In figure 3-27, I show a sequence of flame images corresponding to the quasi-stable mode observed when the fuel bar is located 93 cm upstream of the step; ϕ=0.70, Re=8500, T_{in}=300 K, without hydrogen enrichment. Figure 3-28 shows simultaneous heat release rate, velocity, pressure and equivalence ratio measurements corresponding to the instances shown in figure 3-27. The resonant

frequency is 38 Hz, again corresponding to the quarter wave mode of the combustor. In the quasi-stable case, again a vortex is formed at the edge of the step near the moment of maximum acceleration (2). The vortex grows and convects downstream, forming a pocket of reactants (4-8). Unlike the unstable case, the vortex never grows to reach the top wall, and the reactant pocket is not pinched off by the vortex. The burning is concentrated near the reactant pocket. Compared to the unstable case, the burning of the pocket is not sudden and produces practically no coupled heat release rate fluctuations as shown in figure 3-28. Image (1) and image (8) show approximately the same instance of the cycle, however, the heat release rate is near its maximum and minimum, respectively. This shows that the heat release rate oscillates at a lower frequency than the vortex shedding frequency, indicating the weak coupling between acoustics and the flame dynamics. This results in significantly lower sound pressure levels compared to the unstable mode.

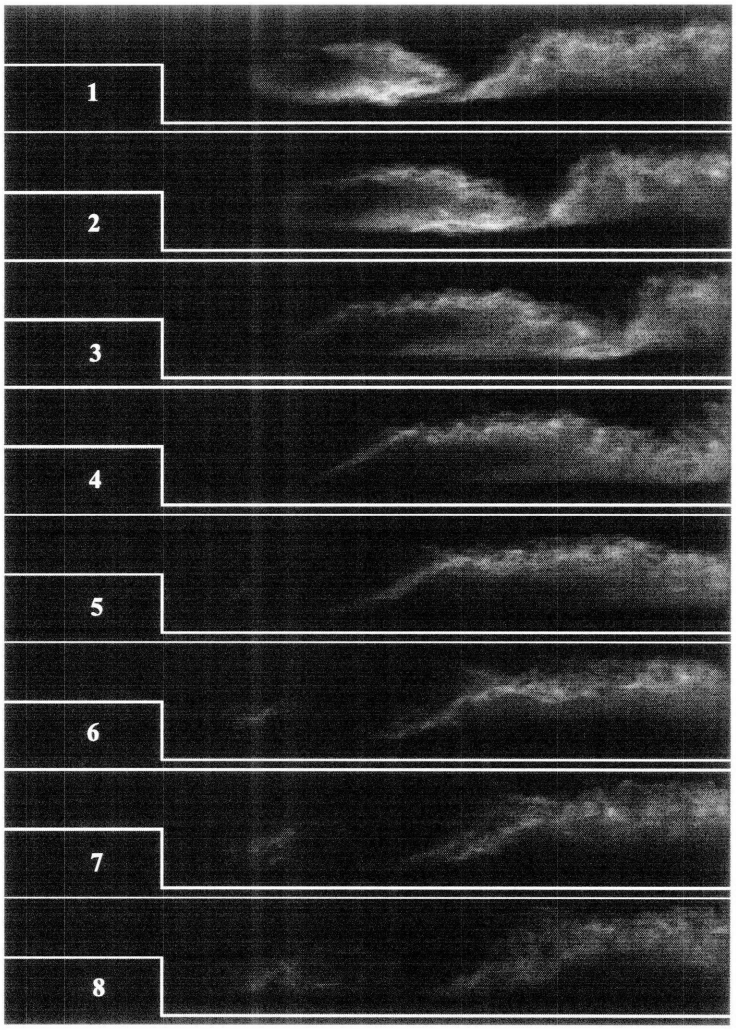

Figure 3-27: Flame images of quasi-stable mode without hydrogen enrichment when the fuel bar is located 93 cm upstream of the step. ϕ=0.70, Re=8500, T_{in}=300 K. The resonant frequency is 38 Hz. The time between frames is 3.8 ms. .

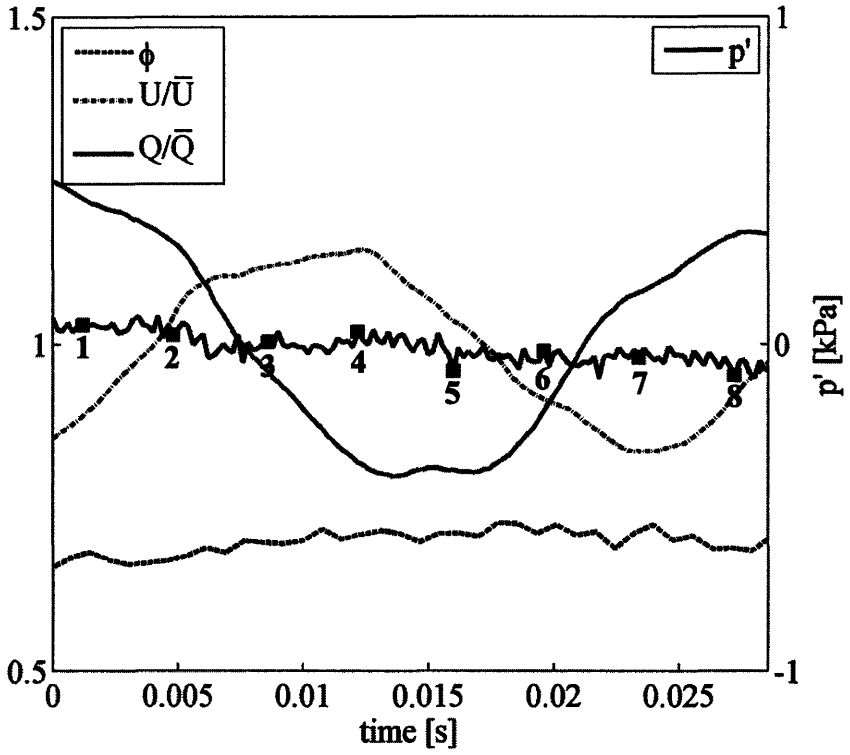

Figure 3-28: Simultaneous heat release rate, velocity, pressure and equivalence ratio measurements corresponding to the quasi-stable mode shown in figure 3-27.

3.6.6 Stable Mode

Very close to the lean flammability limit, the combustor operates in stable mode, resulting in silent burning. As the inlet temperature increases the stable mode becomes narrower and finally disappears when the inlet temperature is 600 K as shown in figure 3-18. In figure 3-29, a sequence of flame images is shown corresponding to the stable mode observed when the fuel bar is located 93 cm upstream of the step; ϕ=0.57, Re=6500, T_{in}=300 K, with 50% by volume hydrogen enrichment. Figure 3-30 shows simultaneous heat release rate, and pressure measurements corresponding to the instances shown in figure 3-29. In the stable case smaller vortices are shed from the step at a higher frequency which does not correspond to the acoustic mode of the

combustor, and thus there is no coupling between heat release rate and pressure as shown in figure 3-30. The heat release rate is steady, and the pressure oscillates at very small amplitude and high frequency, which corresponds to the vortex shedding frequency.

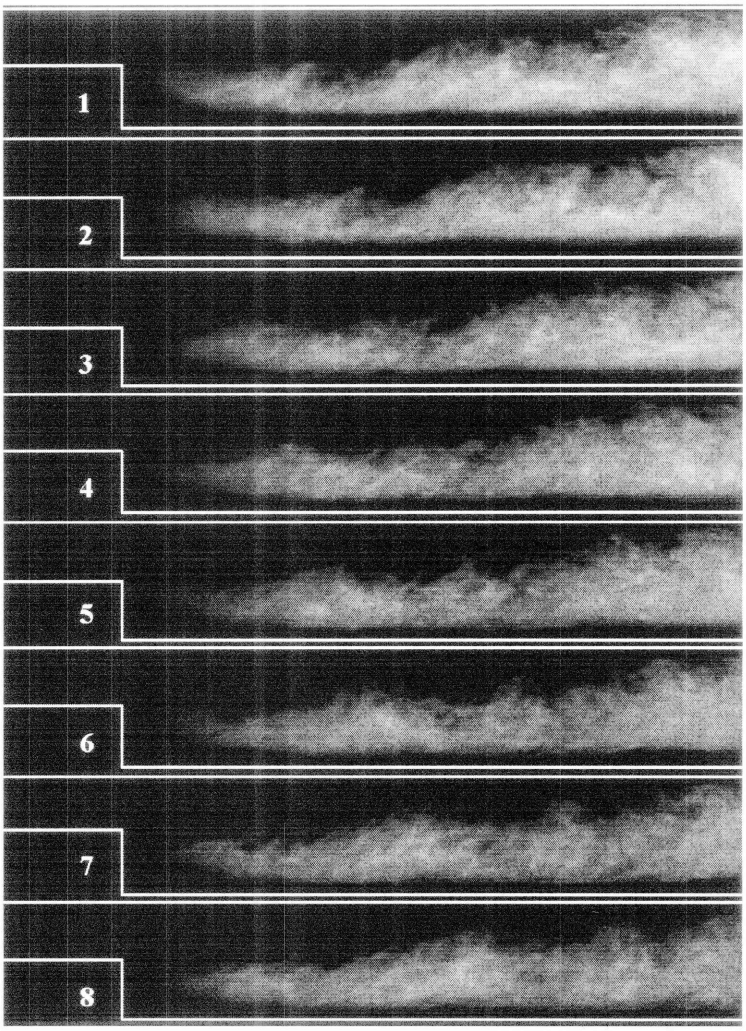

Figure 3-29: Flame images of stable mode with 50% by volume hydrogen enrichment when the fuel bar is located 93 cm upstream of the step. ϕ=0.57, Re=6500, T_{in}=300 K. The time between frames is 4 ms.

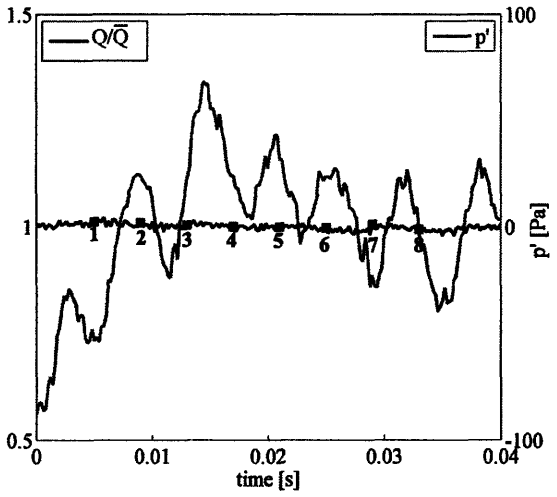

Figure 3-30: Simultaneous heat release rate and pressure measurements corresponding to the stable mode shown in figure 3-29.

3.7 Combustor Acoustics

I measured the pressure along the length of the combustor using 6 pressure sensors installed 0.15 m, 0.76 m, 1.28 m, 2.18 m, 3.07 m and 3.82 m downstream of the choke plate, the positions of which have already been shown in figure 2-6 on page 36. Figure 3-31 shows the root mean square (RMS) pressure oscillation magnitude as a function of the distance from the choke plate for unstable, high frequency unstable, mixed-unstable and quasi-stable modes described above. The sign of the RMS value in this figure is flipped if the phase of the pressure is shifted by more than 90^o due to an acoustic node. I observe that there are two pressure nodes for the high frequency unstable mode. One is between 0.15-0.76 m and the other is between 2.18-3.07 m, which is consistent with the excitation of the higher acoustic mode of the system.

The pressure oscillation amplitude at 0.15 m is lower than than that at 0.76 m both for the unstable and quasi-stable modes; but higher for the mixed unstable mode. This shows the impact of combustion dynamics on the *magnitude* acoustic response

of the combustor. In figure. 3-32, I plot the pressure oscillations against time for the unstable, high frequency unstable, mixed unstable and quasi-stable modes at 0.15 m, 0.76 m, 1.28 m and 3.82 m downstream of the choke plate. The pressure oscillations measured at 0.15 m lags the pressure oscillations measured at 0.76 m around 90^o for the unstable, high frequency unstable, and quasi-stable modes, which is not observed for the mixed unstable mode, which explains the modeshapes shown in figure 3-31. The pressure oscillations measured at 1.28 m and 3.82 m are out-of-phase with each other for the high frequency unstable mode showing the presence of a pressure node at this case as a result of the higher acoustic mode as mentioned above.

From the data shown in figures 3-31 & 3-32 it appears that as the dynamics increase in intensity it is initially the quarter wave mode. The quarter wave mode will oscillate to threshold p'_{rms}. As the dynamics further increase in intensity, they shift to exciting the 3/4 wave mode.

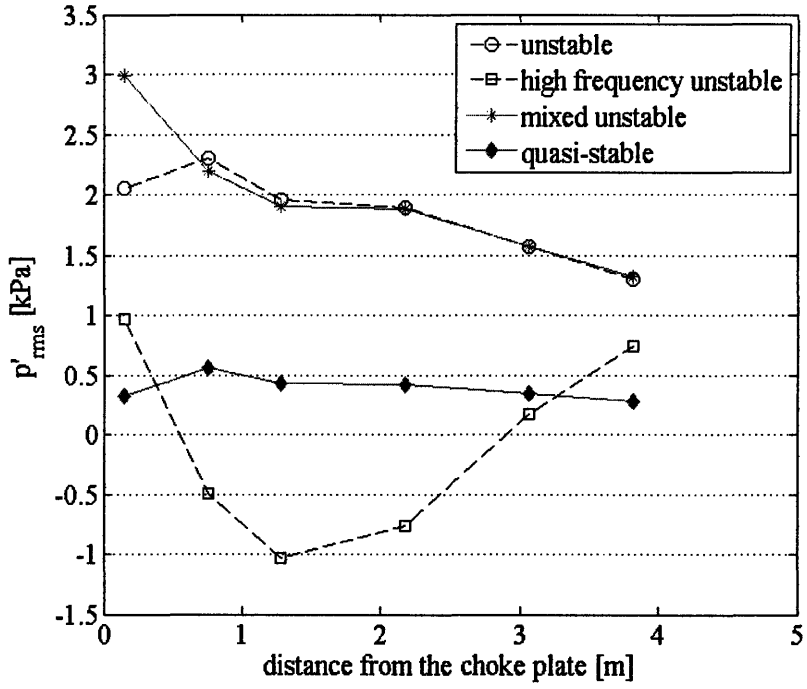

Figure 3-31: RMS pressure oscillation magnitude as a function of the distance from the choke plate for unstable, high frequency unstable, mixed unstable and quasi-stable modes. The sign of the RMS value in this figure is flipped if the phase of the pressure is shifted by more than 90^o due to an acoustic node.

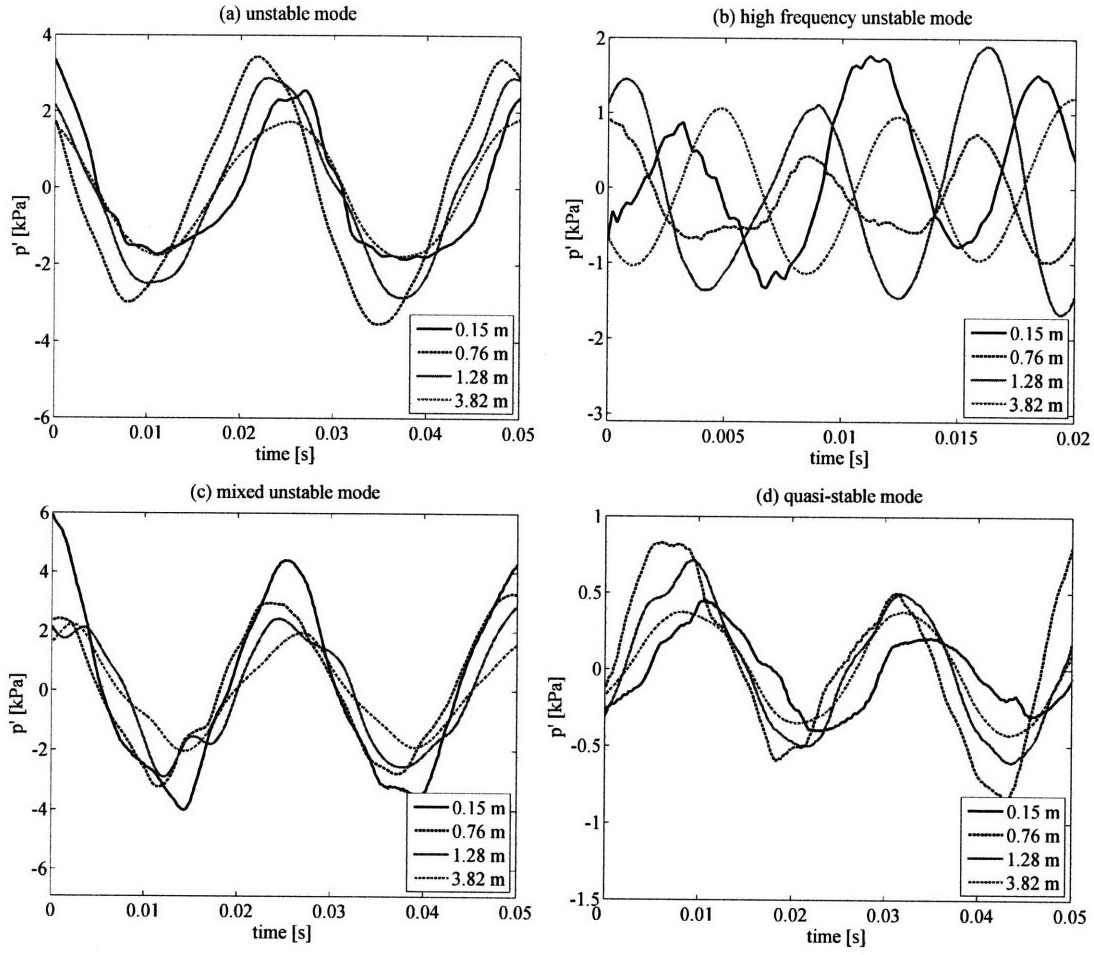

Figure 3-32: Pressure oscillations in time for the (a) unstable (section 3.6.2); (b) high frequency unstable (section 3.6.4); (c) mixed-unstable (section 3.6.3) and (d) quasi-stable modes (section 3.6.5) at 0.15 m, 0.76 m, 1.28 m and 3.82 m downstream of the choke plate.

3.8 Acoustic Instability Suppression Mechanisms

In this thesis I have chosen to focus on the application of choked micro-sized air jets for the suppression of thermoacoustic instabilities. These microjets have the potential to have a high impact on the combustion dynamics with a moderate cost in extra air flow. Both rows of microjets were positioned close to the tip of the step.

In section 3.2 it is shown that the greatest influence the microjets have on the dynamics is by effecting the local velocity field. Considering this, the closer the microjets are to the region to be influenced, the less injected air will need to be utilized. A microjet orientation normal to the main flow was chosen with the goal of disrupting the shear layer, thereby disrupting the wake vortex shedding. The shear layer is at it's most developed at the tip of the step and it is with this awareness that the microjets were drilled at this position.

Another row of microjets were placed on the other side of the step tip facing into the combustion zone, which is seen in figure 2-15 on page 44. These axial microjets were installed following the reasoning described above. Even more so, I reasoned that the axial microjets would have the greatest ability of disrupting the shear layer through this injection method, since most of the microjet momentum that would diffuse into the flow would follow parallel to the shear layer.

In order to show the impact of the microjets on the thermoacoustic instability, the OASPL was measured for a range of equivalence ratios both with microjet flow and without microjet flow. These two stability maps were then compared by subtracting the stability map of the case with the microjets on from the base case with no microjet flowrate as shown

$$\Delta OASPL(\phi) = OASPL_{base}(\phi) - OASPL_{\mu jet}(\phi) \tag{3.2}$$

When $\Delta OASPL$ is positive the microjets have reduced the acoustic noise by the corresponding dB.

3.8.1 Impact of Secondary Air Temperature

The OASPL was measured over a range of equivalence ratios for four cases using propane fuel. Each case in figure 3-33 & 3-34 had a different preheated secondary

air temperature. The main inlet temperature in each figure was kept constant with figure 3-33 at 400 K and figure 3-34 at 600 K. It is observed in these figures first that the axial microjets do not suppress the thermoacoustic instability within a specific range. In figure 3-33 this range varies between $\phi = 0.65$-0.75. In figure 3-34 this range varies between $\phi = 0.55$-0.65. The exact limits of this range have a minor dependence on the secondary air temperature. This range of conditions corresponds to the range of ϕ where the unstable flame front does not flash upstream of the expansion. This is the range of dynamics that is termed in this thesis as the quasi-stable region. A major point to be seen in figures 3-33 & 3-34 is that the preheated secondary air temperature does not have a significant effect on the suppression of the dynamics. There is no clear narrowing of the unstable region or reduction in its amplitude as the temperature of the microjet air is changed. This is an intuitive result, since the mass flowrate of the secondary air is roughly 4% of the main air flowrate. Therefore, one would anticipate any cooling or heating effects of the microjets to be of little impact to the dynamics. This further supports the observations seen in section 3.2 that prove that the major impact of the microjets is their influence on the *velocity field* rather than dilution of the fuel/air mixture.

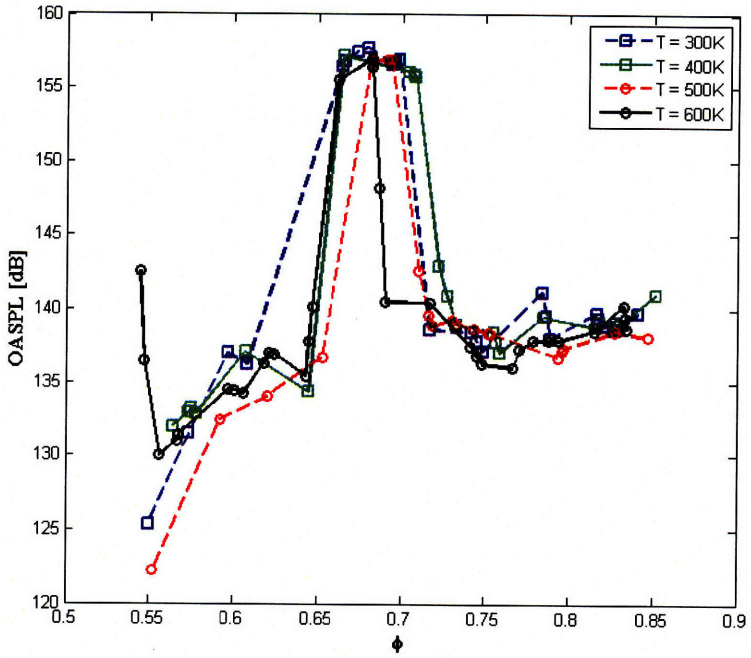

Figure 3-33: OASPL with varying *axial* microjet air temperature at 300 K, 400 K, 500 K and 600 K. The secondary air flowrate is at 1 g/s, T_{in} = 400 K, Re = 6500 and pure propane. The fuel is injected 93 cm upstream of the step and the pressure measurements are taken 1.28 m downstream of the inlet.

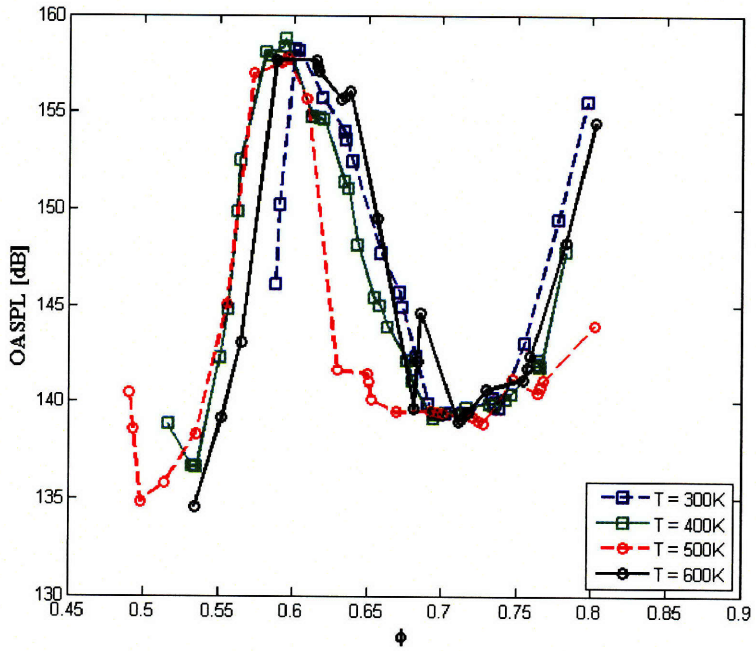

Figure 3-34: OASPL with varying *axial* microjet air temperature at 300 K, 400 K, 500 K and 600 K. The secondary air flowrate is at 1 g/s, T_{in} = 600 K, Re = 6500 and pure propane. The fuel is injected 93 cm upstream of the step and the pressure measurements are taken 1.28 m downstream of the inlet.

3.8.2 Acoustic Suppression with Normal Microjets

In figures 3-35, 3-36 & 3-37 $\Delta OASPL$ is plotted over a range of equivalence ratios with the normal microjets at a different flowrate for each figure. Each figure displays three cases at different inlet air temperatures. In figure 3-35 1 g/s of air is injected through the normal microjets. From this figure one can see that the normal microjets either have very little effect on the OASPL (+/-3 dB) or they reduce it over the ranges shown. The thermoacoustic instability is suppressed across a narrow range with a varying degree for each case. This range of suppression is indicated by the peak of each $\Delta OASPL$ curve. This range moves towards a leaner range of equivalence ratios as T_{in} is increased.

These cases are repeated in figure 3-36 with a normal microjet flowrate of 1.5 g/s. In this figure the magnitude of the reduction for inlet temperatures of 500 K and 600 K have reduced whereas the reduction has increased to around 5 dB for the 400 K case between ϕ = 0.6-0.7. The normal microjets actually *increase* the OASPL by 10 dB near the higher equivalence ratios at T_{in} = 600 K.

When the normal microjet flowrate is increased to 2 g/s, seen in figure 3-37, the reduction curve has not changed much for the 400 K case. The 500 K case has reverted back to the reduction curve seen in figure 3-35, but the 600 K case now has a 18 dB reduction in the OASPL around ϕ = 0.55. Under the conditions observed in these three figures it can be seen that the range of suppression for each case is narrow and the $\Delta OASPL$ is typically between 5-10 dB. As in figure 3-36 the normal microjets at 2 g/s increase the OASPL near the higher equivalence ratios at the 600 K case and they also increase the OASPL near the lean blowout limit.

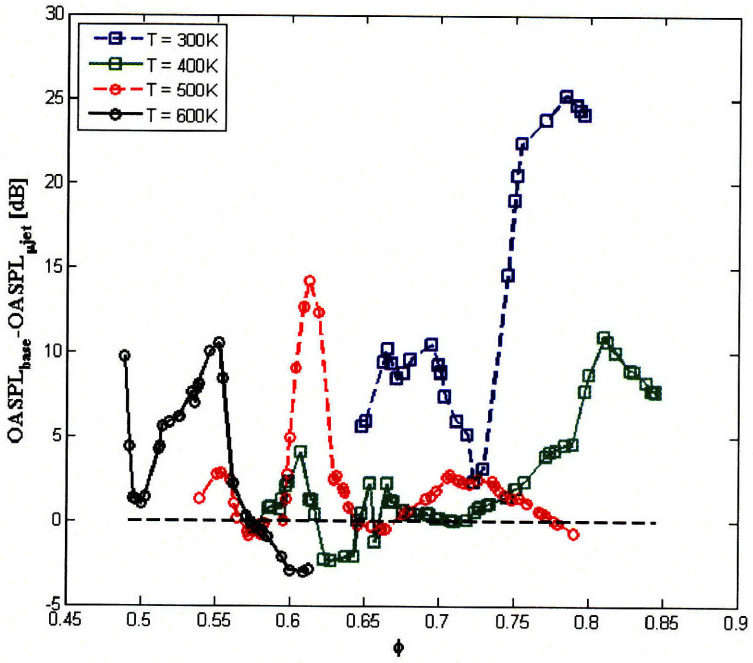

Figure 3-35: OASPL reduction with 1 g/s of *normal* microjet flowrate at three different inlet temperatures of 400 K, 500 K and 600 K. The secondary air temperature matches T_{in}, Re = 6500 and the fuel is pure propane. The fuel is injected 93 cm upstream of the step and the pressure measurements are taken 1.28 m downstream of the inlet.

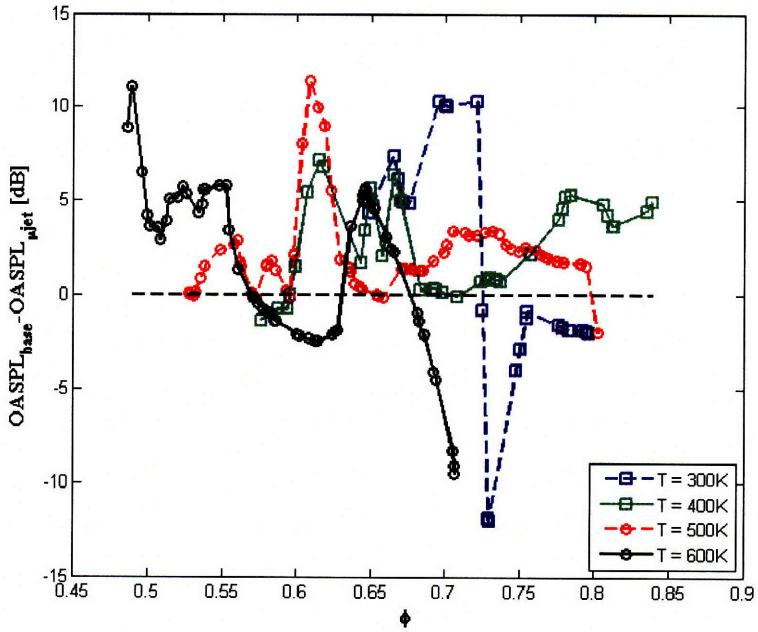

Figure 3-36: OASPL reduction with 1.5 g/s of *normal* microjet flowrate at three different inlet temperatures of 400 K, 500 K and 600 K. The secondary air temperature matches T_{in}, Re = 6500 and the fuel is pure propane. The fuel is injected 93 cm upstream of the step and the pressure measurements are taken 1.28 m downstream of the inlet.

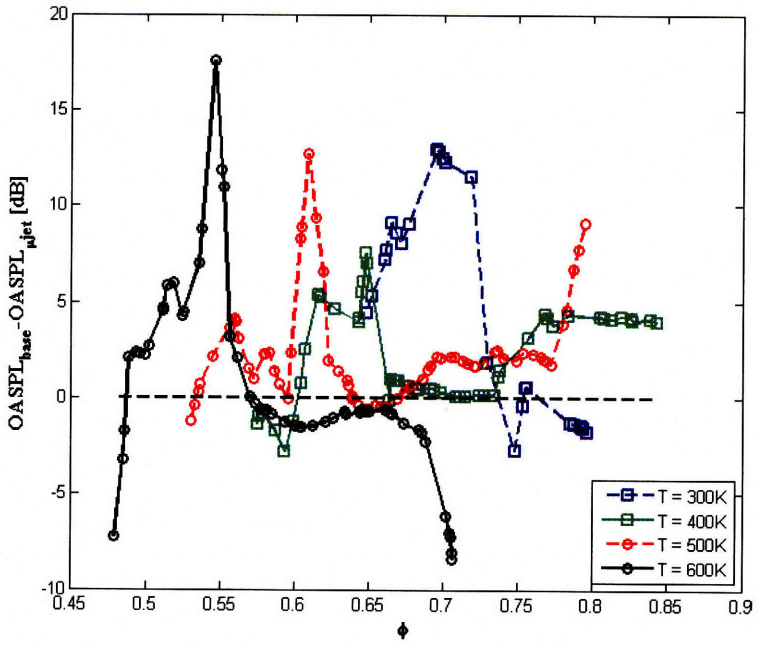

Figure 3-37: OASPL reduction with 2 g/s of *normal* microjet flowrate at three different inlet temperatures of 400 K, 500 K and 600 K. The secondary air temperature matches T_{in}, Re = 6500 and the fuel is pure propane. The fuel is injected 93 cm upstream of the step and the pressure measurements are taken 1.28 m downstream of the inlet.

3.8.3 Effect of H_2 Addition with Normal Microjets

The normal microjets were tested with 50% H_2 by volume added to the fuel and 1.5 g/s of secondary air flowrate. The $\Delta OASPL$ curve was found at these conditions for three different inlet air temperatures and the results are shown in figure 3-38. It can be seen from this figure that the normal microjets have a much greater impact on the suppression of the thermoacoustic instability when there is H_2 added to the fuel. There is a range at 500 K where the normal microjets increase the acoustic instability in the combustor by around 8 dB between ϕ = 0.65-0.7. This instability increase also occurs for the 600 K case at around ϕ = 0.55.

In figure 3-39 the OASPL is recorded over a range of equivalence ratios for four cases, each with 1.5 g/s of normal microjet flowrate. For each case the data point at the lowest equivalence ratio indicates the lean blowout limit. The four cases are meant to compare the effects of inlet temperature and H_2 content on the normal microjet stability maps. The H_2 addition shifts the stability curve to leaner equivalence ratios for each inlet temperature as expected. The H_2 cases also have a wider and more intense range of instability than the pure propane cases. Even though this is the case, there is still a greater reduction over the range of OASPL with H_2 than with pure propane.

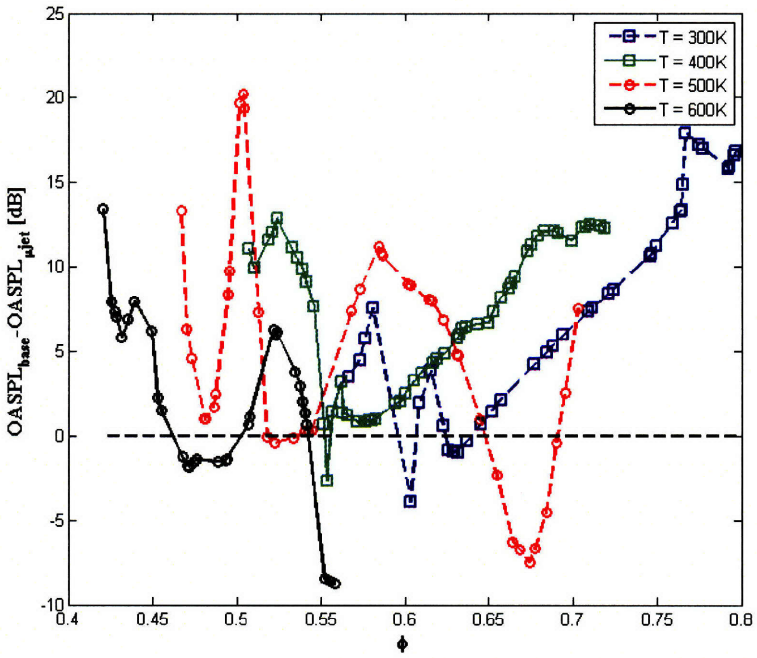

Figure 3-38: OASPL reduction with 1.5 g/s of *normal* microjet flowrate at three different inlet temperatures of 400 K, 500 K and 600 K. The secondary air temperature matches T_{in}, Re = 6500 and the fuel is 50% H_2 by volume. The fuel is injected 93 cm upstream of the step and the pressure measurements are taken 1.28 m downstream of the inlet.

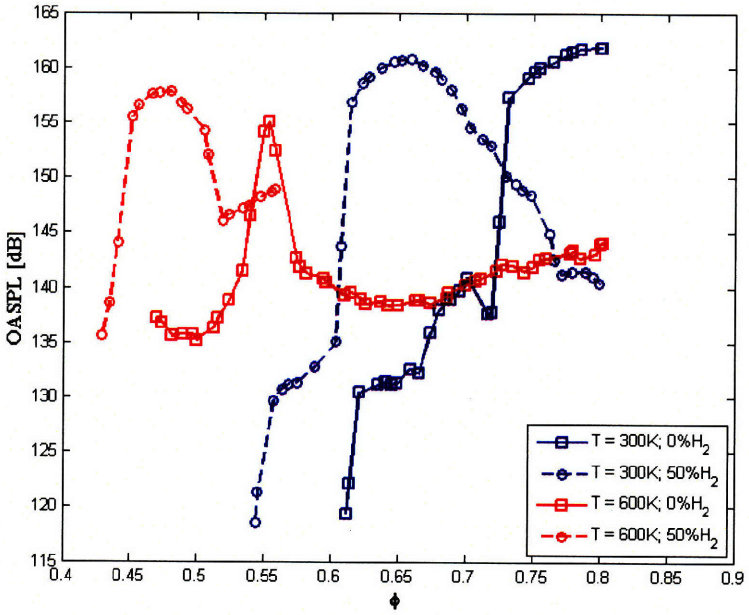

Figure 3-39: OASPL with 1.5 g/s of *normal* microjet flowrate at two different inlet temperatures of 400 K and 600 K and two different fuel concentrations of 0% and 50% H_2 by volume. The secondary air temperature matches T_{in} and Re = 6500. The fuel is injected 93 cm upstream of the step and the pressure measurements are taken 1.28 m downstream of the inlet.

3.8.4 Acoustic Suppression with Axial Microjets

In the figures 3-40,3-41 & 3-42 $\Delta OASPL$ is shown over a range of equivalence ratios and four cases at different inlet air temperatures. For each case the secondary air temperature was preheated to match the inlet temperature. From the data shown in figure 3-40 it can be seen that over all four cases the axial microjets either have little effect or the suppress instabilities except over a small range between ϕ = 0.72-0.74 at 300 K inlet temperature. The case with a temperature at 300 K is the least relevant since it is the furthest from typical industrial conditions. The case with the widest range of suppression in figure 3-40 is the case with 500 K inlet temperature where the typical $\Delta OASPL$ is greater than 10 dB. At 400 K inlet temperature the

$\Delta OASPL$ is even greater within the active range of suppression. When the dynamics are suppressed the $\Delta OASPL$ is typically between 15-20 dB. There is a more erratic level of suppression over smaller separate ranges of ϕ for the 600 K inlet temperature case, but this changes quickly as shown in figure 3-41 where the axial microjet flowrate is increased to 1.5 g/s.

At 1.5 g/s of axial microjet flowrate, seen in figure 3-41, the axial microjets become much more effective at suppressing the thermoacoustic instability when the inlet air temperature is at 600 K. The major range of suppression for this case has been shifted and widened from $\phi = 0.53$-0.57 to $\phi = 0.55$-0.68, with the $\Delta OASPL$ now at a constant 15 dB. The 300 K case has retained the same range of suppression, but the $\Delta OASPL$ has halved compared to figure 3-40. Between $\phi = 0.71$-0.74 where the thermoacoustic instability is increased, the level of acoustic amplification has doubled when compared with figure 3-40. The range of suppression for the 400 K case has widened from $\phi = 0.71$-0.83 to $\phi = 0.67$-0.83 making the axial microjets effective at lower equivalence ratios. There is no major difference in the suppression range for the 500 K case when comparing 1 g/s to 1.5 g/s of axial microjet air injection.

In figure 3-42 at 2 g/s of axial microjet flowrate the gains in suppression start to become counterbalanced by conditions where the instability is intensified. For the 400 K, 500 K and 600 K cases the instability is intensified within the range that would be the *stable mode* if the microjets were off. The range of positive suppression for these cases has not changed, but the magnitude of the $\Delta OASPL$ is not as high as what is shown in figure 3-41. The 300 K case has reverted back to the $\Delta OASPL$ curve seen for the 1 g/s axial microjet flowrate, except there is a major suppression of noise at $\phi = 0.77$ on the order of 40 dB.

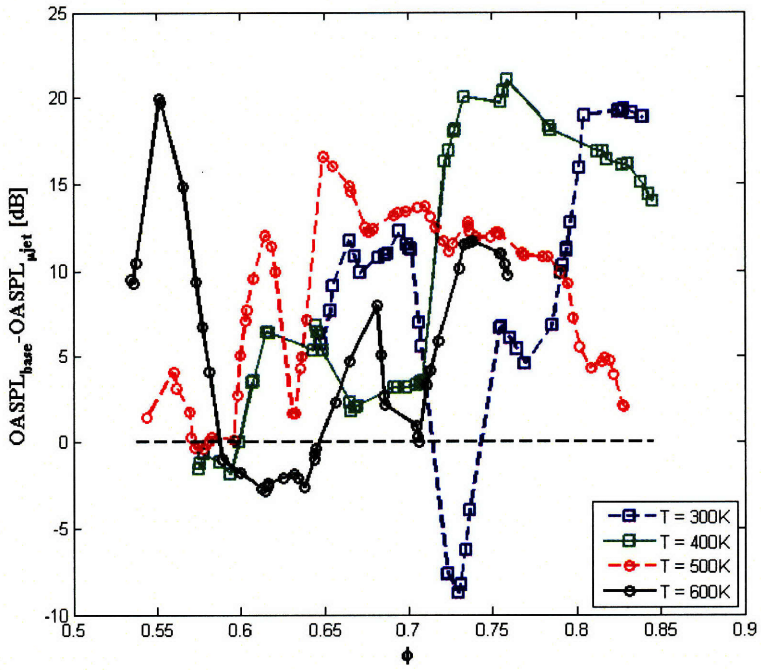

Figure 3-40: OASPL reduction with 1 g/s of *axial* microjet flowrate at three different inlet temperatures of 400 K, 500 K and 600 K. The secondary air temperature matches T_{in}, Re = 6500 and the fuel is pure propane. The fuel is injected 93 cm upstream of the step and the pressure measurements are taken 1.28 m downstream of the inlet.

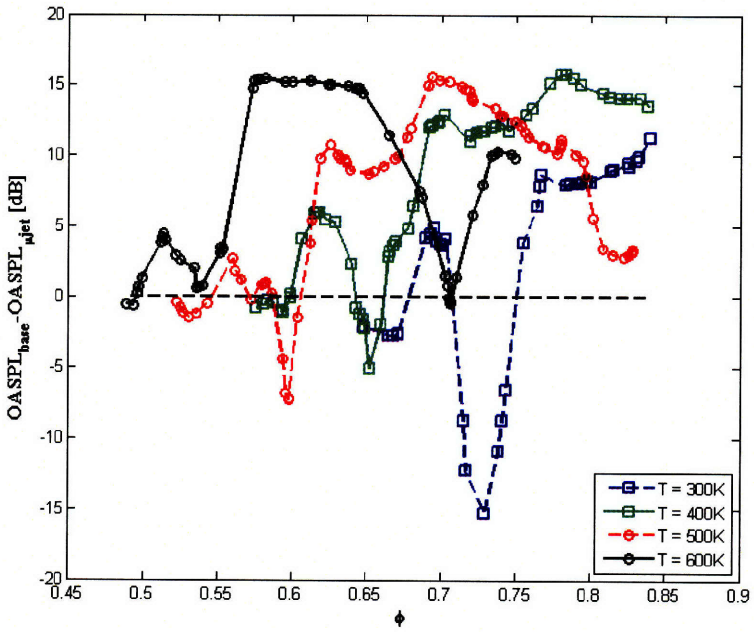

Figure 3-41: OASPL reduction with 1.5 g/s of *axial* microjet flowrate at three different inlet temperatures of 400 K, 500 K and 600 K. The secondary air temperature matches T_{in}, Re = 6500 and the fuel is pure propane. The fuel is injected 93 cm upstream of the step and the pressure measurements are taken 1.28 m downstream of the inlet.

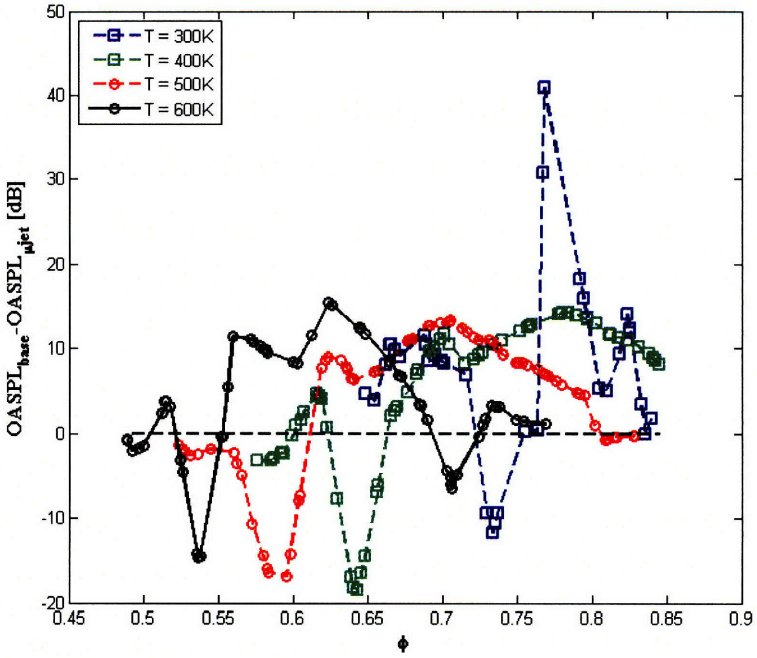

Figure 3-42: OASPL reduction with 2 g/s of *axial* microjet flowrate at three different inlet temperatures of 400 K, 500 K and 600 K. The secondary air temperature matches T_{in}, Re = 6500 and the fuel is pure propane. The fuel is injected 93 cm upstream of the step and the pressure measurements are taken 1.28 m downstream of the inlet.

3.8.5 Effect of H_2 Addition with Axial Microjets

It was observed that the axial microjets were equally if not even more effective at suppressing combustion instability after H_2 was added to the fuel. To illustrate this two cases were taken where $\Delta OASPL$ is plotted over a range of equivalence ratios with 50% H_2 by volume was added to the fuel, which is shown in figure 3-43. Each case has a different inlet air temperature with a matching secondary air temperature. As expected the measured range of $\Delta OASPL$ for each case is leaner than the cases seen in figure 3-41 due to the hydrogen addition. At 1.5 g/s there is a positive suppression of the thermoacoustic instability over the entire measured range for 300K inlet temperature. Except for a range between ϕ = 0.6-0.7, the typical $\Delta OASPL$

is on the order of 15 dB. With the 600 K case the is also mostly suppressed with a typical $\Delta OASPL$ between 10-15 dB.

The stability map was taken for four cases to compare the effect of hydrogen addition when axial microjets are kept at a constant flowrate. As shown in figure 3-44 all of the cases have 1 g/s secondary air flowrate with a secondary air temperature that matches the main inlet temperature. The measurement at the lowest equivalence ratio for each case indicates the lean blowout limit for the corresponding inlet parameters. It is seen that the stability map maintains its characteristic shape even with the axial microjets on, but as expected from the tests given in section 3.5, this curve is shifted to leaner equivalence ratios. For the case with 600 K inlet and 50% H_2 thermoacoustic instability appears to be non-existed up until $\phi = 0.68$. This appears to be a convergence of the benefits of both H_2 addition coupled with axial microjet injection. Except for this case the axial microjets to do not appear to be able to suppress the instability for the region corresponding to the quasi-stable case described in section 3.6.5.

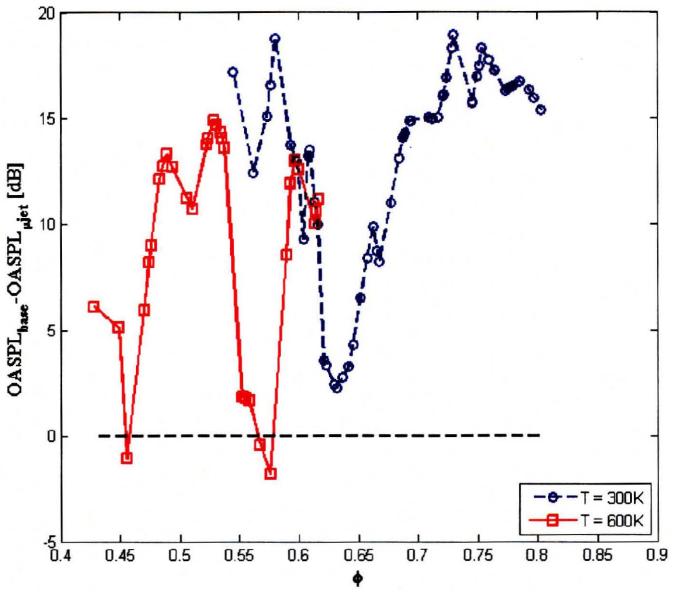

Figure 3-43: OASPL reduction with 1.5 g/s of *axial* microjet flowrate at three different inlet temperatures of 300 K and 600 K. The secondary air temperature matches T_{in}, Re = 6500 and the fuel is 50% H_2 by volume. The fuel is injected 93 cm upstream of the step and the pressure measurements are taken 1.28 m downstream of the inlet.

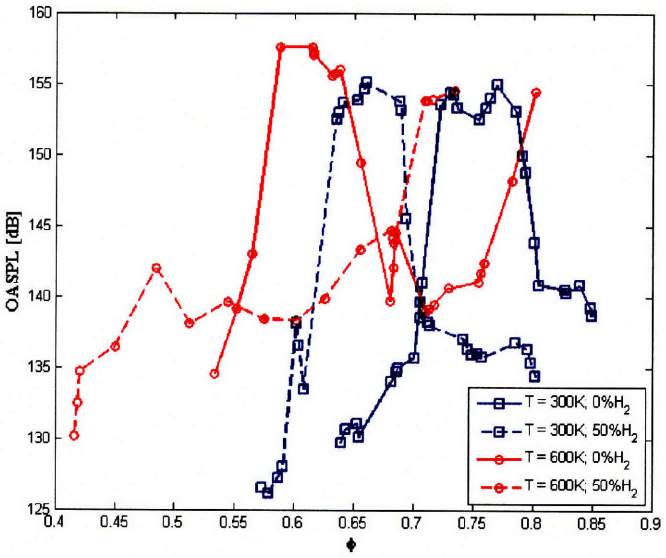

Figure 3-44: OASPL with 1 g/s of *axial* microjet flowrate at two different inlet temperatures of 300 K and 600 K and two different fuel concentrations of 0% and 50% H_2 by volume. The secondary air temperature matches T_{in} and Re = 6500. The fuel is injected 93 cm upstream of the step and the pressure measurements are taken 1.28 m downstream of the inlet.

3.8.6 Combustion Dynamics with Microjets

High speed video was taken of cases recording the change in dynamics due to 1.5 g/s of microjet flowrate at 600 K inlet temperature for both microjet injection methods. All of the cases have 600 K preheated secondary air to match the main inlet air temperature and avoid any possibility of the flame dynamics being effected by minor cooling.

3.8.6.1 Stable Dynamics

In figure 3-45 the flame dynamics at $\phi = 0.53$ are shown for stable dynamics as described in section 3.6.6. In figure 3-46 the dynamics are shown for the same conditions except with 1.5 g/s of normal microjet injection. There does not appear to be

a significant change in the OASPL after the normal microjets are activated in this case. Neither do the dynamics appear to have changed any noticeable degree. Figure 3-47 shows flame dynamics at the same input conditions, but with the addition of 1.5 g/s of axial microjet flowrate. With the axial microjet injection the flame sheet is no longer anchored to the tip of the step. The products side of the flame is on the top side rather than the bottom side. There is also a 5 dB increase in the OASPL when compared to the case without microjets. In all three of these cases the lack of reduction in OASPL is acceptable, because the OASPL for these cases are all within the stable regime. It would have been unacceptable with regards to the performance had the microjets caused a 10 dB or greater *increase* in the OASPL.

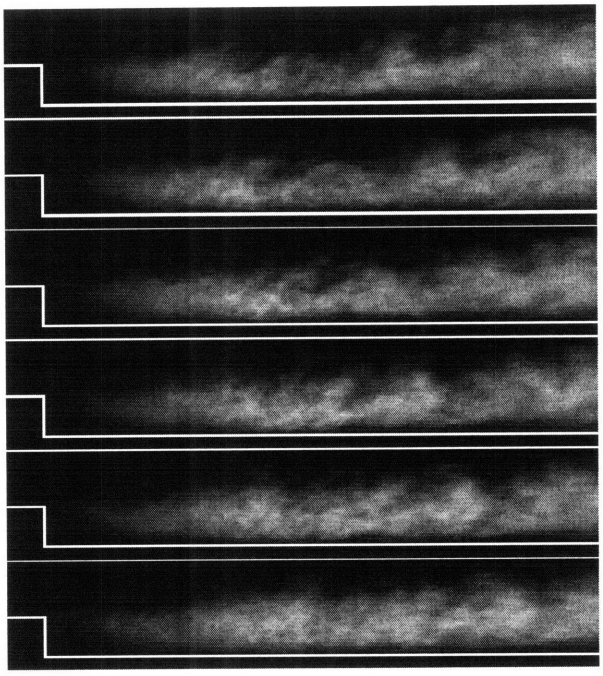

Figure 3-45: Flame shape at 600 K inlet temperature, $\phi = 0.53$. Time between frames is 10 ms and OASPL = 139 dB. The fuel is injected 93 cm upstream of the step and the fuel is pure propane.

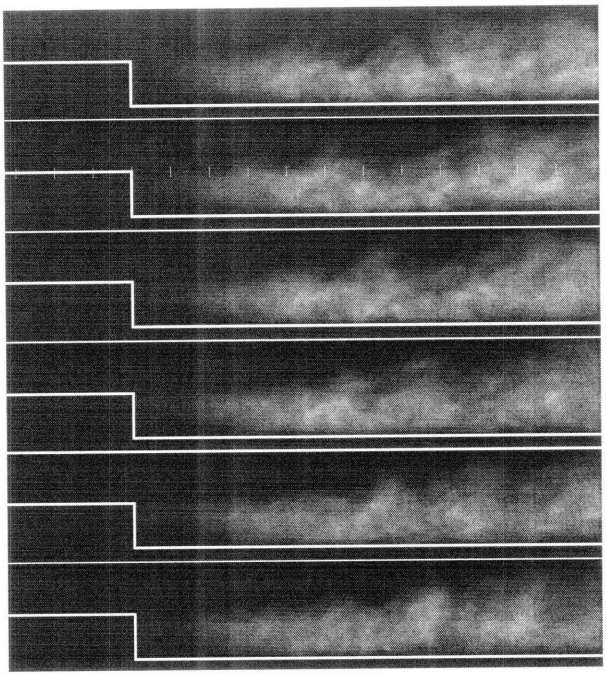

Figure 3-46: Flame shape at 1.5 g/s *normal* microjet flowrate at 600 K inlet temperature, $\phi = 0.53$. Time between frames is 10 ms and OASPL = 141 dB. The fuel is injected 93 cm upstream of the step and the fuel is pure propane.

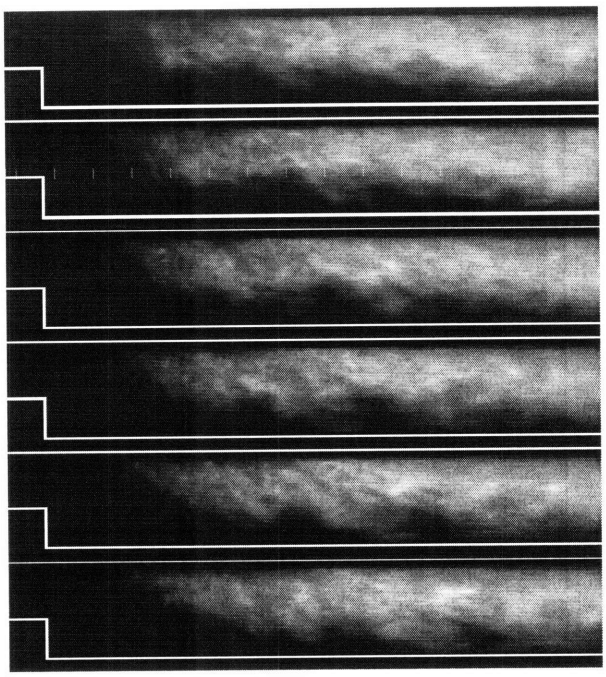

Figure 3-47: Flame shape at 1.5 g/s *axial* microjet flowrate at 600 K inlet temperature, $\phi = 0.53$. Time between frames is 10 ms and OASPL = 144 dB. The fuel is injected 93 cm upstream of the step and the fuel is pure propane.

3.8.6.2 Quasi-stable Dynamics

Figure 3-48 presents high speed video images of the flame dynamics at $\phi = 0.57$. At this input condition the flame front is distorted by the wake vortex shedding from the edge of the step. With 1.5 g/s of normal microjet flowrate, seen in figure 3-49, the flame sheet is more turbulent than it is in figure 3-48, but there is no significant change in the OASPL.

The axial microjets do appear to have significant impact on the flame shape. Once the axial microjets are activated with 1.5 g/s of air flow, the dynamics change to what is seen in figure 3-50 where the flame front is no longer anchored on the tip of the step. The flame sheet has more pronounced flamelets due to the additional turbulence introduced by the microjets. Most noticeable is the lack of the distinct wake vortex shape that is present in figure 3-48. Even with the change in the flame dynamics

there is no reduction in the OASPL due to the axial microjet injection.

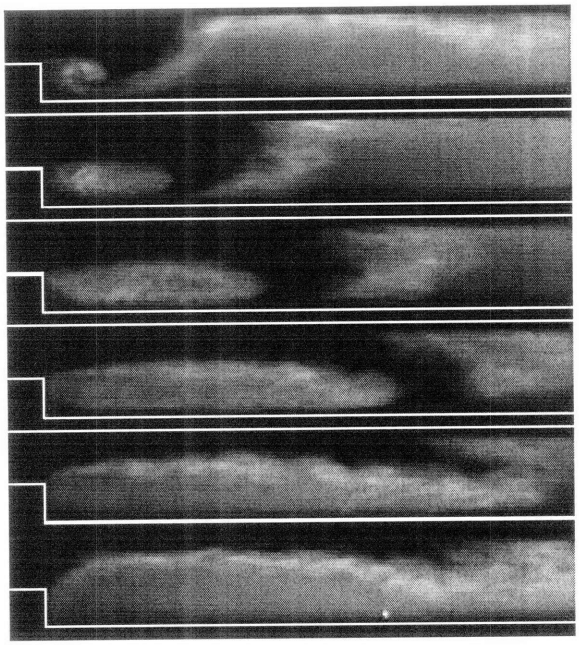

Figure 3-48: Flame shape at 600 K inlet temperature, $\phi = 0.57$. Time between frames is 27 ms and OASPL = 159 dB. The fuel is injected 93 cm upstream of the step and the fuel is pure propane.

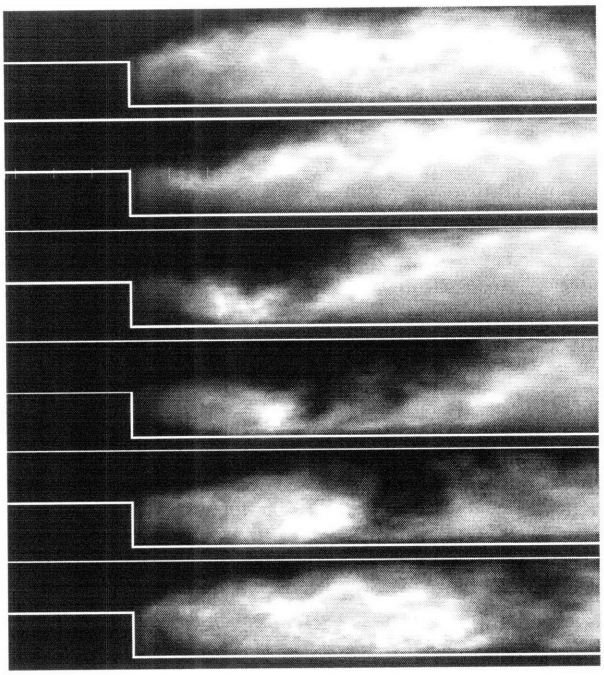

Figure 3-49: Flame shape at 1.5 g/s *axial* microjet flowrate at 600 K inlet temperature, $\phi = 0.57$. Time between frames is 30 ms and OASPL = 157 dB. The fuel is injected 93 cm upstream of the step and the fuel is pure propane.

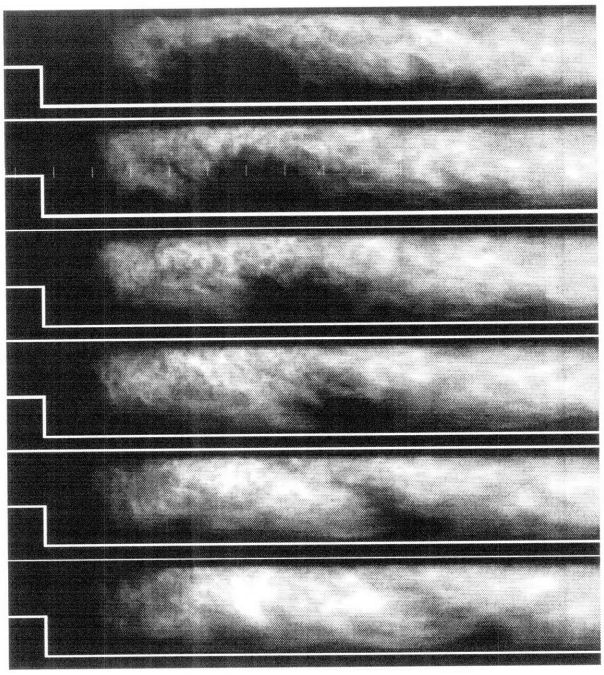

Figure 3-50: Flame shape at 1.5 g/s *axial* microjet flowrate at 600 K inlet temperature, $\phi = 0.57$. Time between frames is 10 ms and OASPL = 159 dB. The fuel is injected 93 cm upstream of the step and the fuel is pure propane.

3.8.6.3 Unstable Dynamics

Figures 3-51, 3-49 & 3-53 compare the effect of the microjets on the combustion dynamics with $\phi = 0.66$. The microjet flowrate for both types is 1.5 g/s. The flame dynamics without microjets at this case is very similar to those in figure 3-48. When the normal microjets are turned on in figure 3-52 the periodic wake vortex shedding, which is seen in figure 3-51 is no longer present. This change in the flame dynamics does not appear to have a suppressing effect on the OASPL. It is further seen that it is the axial microjets which are capable of suppressing the thermoacoustic instability at this condition.

When the axial microjets are turned on the shape of the flame sheet is no longer dominated by wake vortex shedding and becomes stationary and much more compact. This has the effect of producing a high heat flux on the combustor wall at the bottom

inner corner of the step. This flame shape is shown in figure 3-53. The effect of the axial microjets is clearly visible by the angled tip of the flame sheet in front of the injection site. This angled flame shape is expected from observing the velocity profile in figure 3-10 in section 3.2, where the local velocity is highest in front of the microjet injection site and decreases towards the upper and lower walls. The recirculation zone becomes roughly half the size of vortexes formed in figure 3-51 and the flame within this recirculation zone loses its clear definition, reminding one of a well-stirred reactor. One sees a 11 dB reduction in the OASPL caused by the axial microjets when comparing the case without microjets to the case with microjets on.

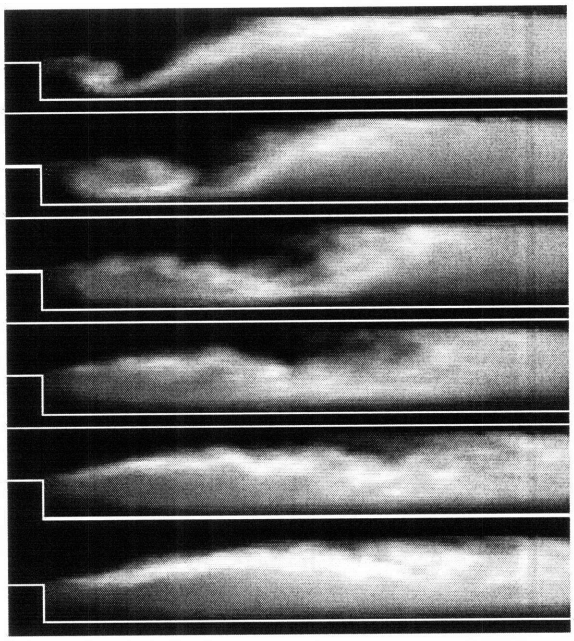

Figure 3-51: Flame shape at 600 K inlet temperature, $\phi = 0.66$. Time between frames is 20 ms and OASPL = 150 dB. The fuel is injected 93 cm upstream of the step and the fuel is pure propane.

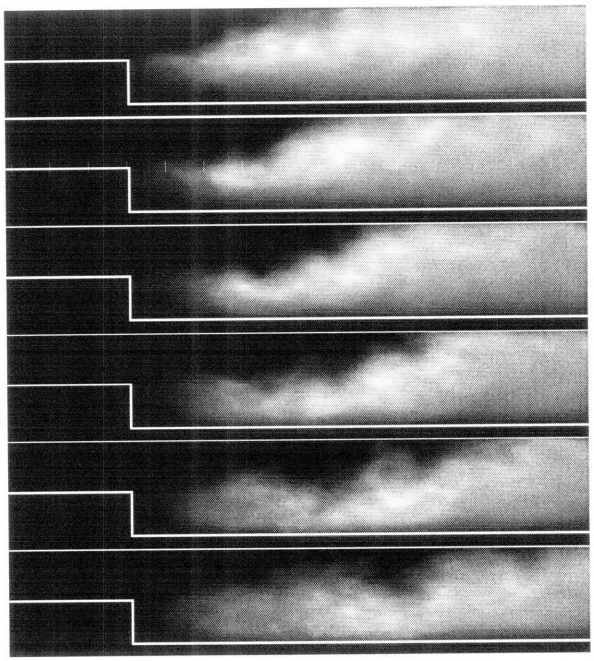

Figure 3-52: Flame shape at 1.5 g/s *normal* microjet flowrate at 600 K inlet temperature, $\phi = 0.66$. Time between frames is 18 ms and OASPL = 153 dB. The fuel is injected 93 cm upstream of the step and the fuel is pure propane.

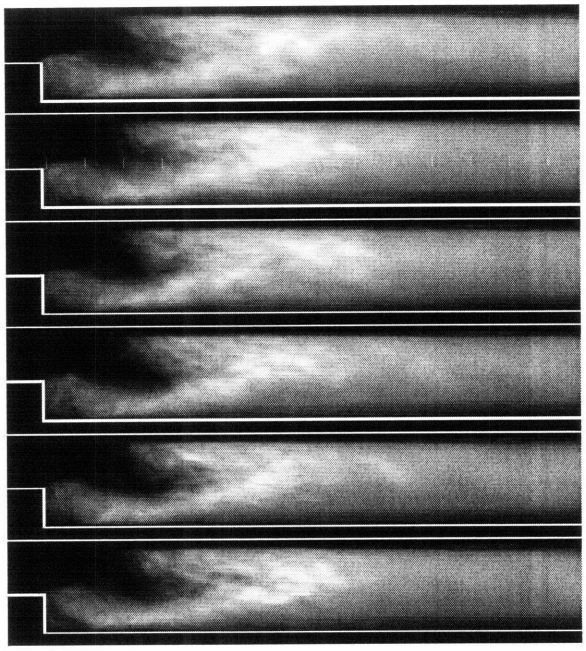

Figure 3-53: Flame shape at 1.5 g/s *axial* microjet flowrate at 600 K inlet temperature, ϕ = 0.66. Time between frames is 10 ms and OASPL = 139 dB. The fuel is injected 93 cm upstream of the step and the fuel is pure propane.

3.8.6.4 High Frequency Unstable Dynamics

In figures 3-54, 3-55 & 3-56 the microjets are tested for 1.5 g/s of secondary air at ϕ = 0.78 and an inlet temperature of 600 K. At this set of inlet conditions the dominant frequency of the thermoacoustic instability is 137 Hz. This higher frequency is the cause of the smaller wake vortexes being shed from the step edge that one sees in figure 3-54. When the normal microjets are turned on, one sees in figure 3-55 that flame sheet has similar dynamics to the case without the microjets, but these dynamics are even more compact. In this case to dominant acoustic frequency is 205 Hz, which corroborates the compact dynamics. This has the unfortunate effect of increasing the OASPL by 4 dB.

Despite the high frequency of the instability the axial microjets still stabilize the flame by fundamentally altering the velocity field. The flame dynamics after axial

microjet injection are shown in figure 3-56 and one can see identical behavior to that shown in figure 3-53. When comparing the case with axial microjet injection to the case without axial microjet injection, the axial microjets suppress the OASPL by 9 dB at these inlet conditions.

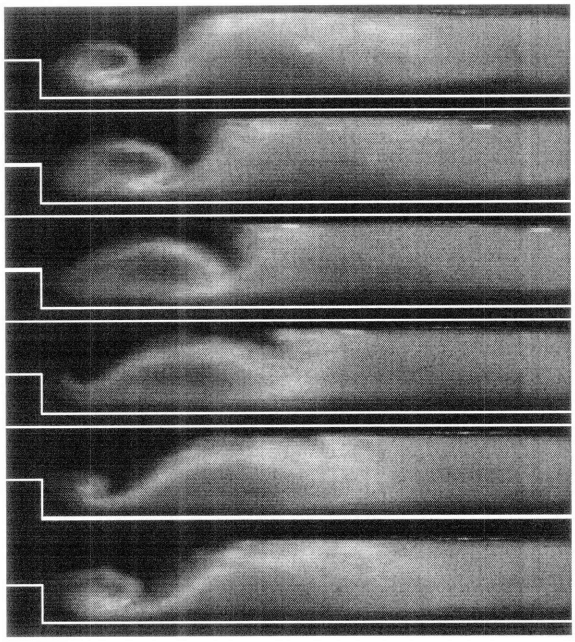

Figure 3-54: Flame shape at 600 K inlet temperature, $\phi = 0.78$. Time between frames is 10 ms and OASPL = 152 dB. The fuel is injected 93 cm upstream of the step and the fuel is pure propane.

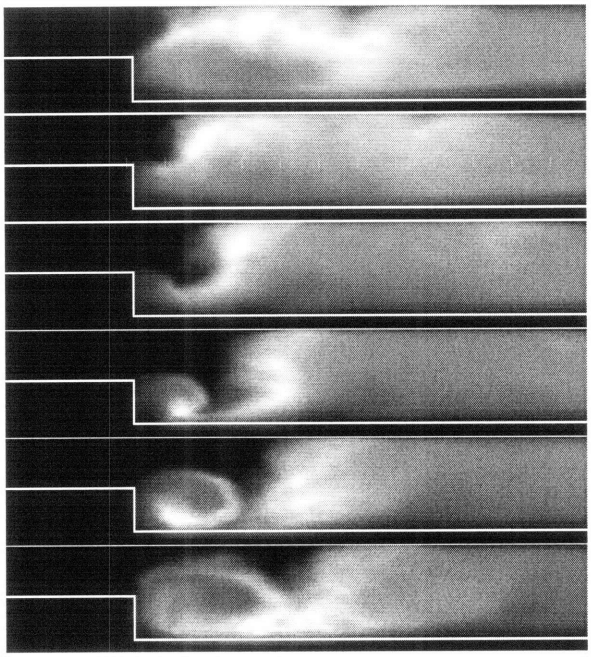

Figure 3-55: Flame shape at 1.5 g/s *normal* microjet flowrate at 600 K inlet temperature, $\phi = 0.78$. Time between frames is 10 ms and OASPL = 156 dB. The fuel is injected 93 cm upstream of the step and the fuel is pure propane.

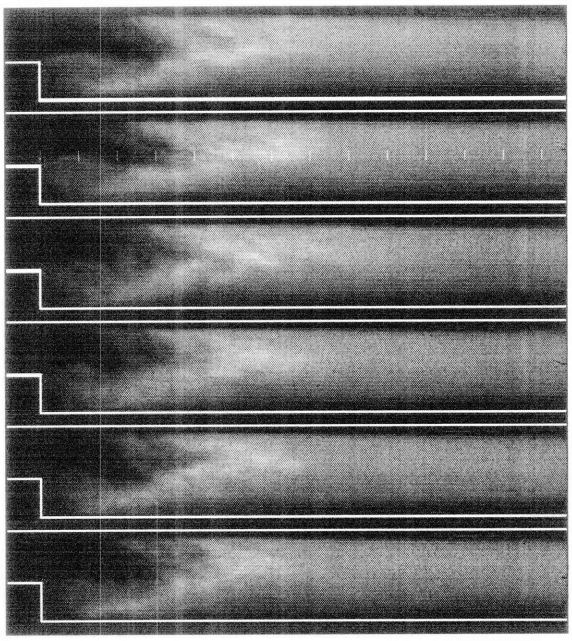

Figure 3-56: Flame shape at 1.5 g/s *axial* microjet flowrate at 600 K inlet temperature, $\phi = 0.78$. Time between frames is 25 ms and OASPL = 143 dB. The fuel is injected 93 cm upstream of the step and the fuel is pure propane.

Chapter 4

Conclusions

The ability to fully characterize combustion dynamics is invaluable to understanding the mechanisms that provoke and sustain thermoacoustic instability. By having a greater understanding of these mechanisms it is possible to design combustors with a wider range operability. This knowledge also reduces the time to design a combustor by eliminating options from a trial-and-error design approach. I was able to achieve a full parametric characterization of the combustor through the simultaneous measurement of the perturbations of pressure, velocity, heat release, and equivalence ratio. These measurements were further supported through the use of a digital high speed camera.

I systematically investigated the stability map and combustion dynamics in a backward-facing step combustor. Simultaneous pressure, velocity, heat release rate and equivalence ratio measurements and high-speed video from the experiments are used to identify and characterize several distinct operating modes. The combustion dynamics are governed by both flame-vortex interactions and the equivalence ratio oscillations. Changing the location of the fuel injector, I concluded that flame-vortex interactions were the dominant mechanism.

When equivalence ratio oscillations were not present, I observed four distinct oper-

ating modes of the combustor depending on the inlet temperature and the equivalence ratio. At high equivalence ratios, the combustor is unstable as a result of the strong interaction between the large unsteady wake vortex and the flame. At intermediate equivalence ratios, the combustor is quasi-stable where a typical shear layer instability is observed. Near the flammability limit, long stable flames are observed. When the inlet temperature is atmospheric, the quasi-stable and the unstable flames couple with the quarter wavemode of the combustor. When the inlet temperature is increased, at high equivalence ratios, 3/4 wavemode of the combustor is excited, tripling the oscillation frequency. This operating mode is the high frequency unstable mode, where the flame is more compact compared to the unstable case.

When equivalence ratio oscillations are present, I did not observe the stable and quasi-stable modes. The flame is unstable at the entire range of equivalence ratios, and its dynamics are governed by both of the mechanisms. This is the mixed unstable operating mode of the combustor. The lean flammability limit is higher than the cases without equivalence ratio oscillations, since the instantaneous equivalence ratio during part of the cycle becomes very small, causing the flame to blowout. Increasing the inlet temperature and hydrogen concentration shifts the gain curves of the combustor towards lower equivalence ratios. As the inlet temperature is increased, the stable operating band gets narrower, and finally disappears when the inlet temperature is 600 K.

Understanding the mechanisms which govern combustion dynamics is critical to designing stable combustors, but any combustor design will be limited by these basic mechanisms. In order to overcome the limits of a combustors fundamental stability limits requires adding additional mechanisms to the system that are capable of extending this stability limit. I experimented with two mechanisms using microjet injection of air. The normal microjets were found to have only a minor effect at suppressing instabilities under the conditions tested. Under certain conditions the

normal microjets would suppress the thermoacoustic instability, but this range was narrow and hysteresis effects would influence the exact position of this range. The axial microjets proved to be much more effective at an optimal flowrate of around 1.5 g/s. This microjet configuration was very reliable at preventing the collapse of the wake vortexes shed from the step due to their pronounced ability to distort the flow field downstream of the step. Although the axial microjets were effective across the entire range of unstable dynamics, they were not as reliable near the quasi-stable dynamic regions. The axial microjets were not effective below 1 g/s and as the flowrate is increased above 1.5 g/s they are not as effective. If one increases the axial microjet flow rate above 2 g/s they will increase the instability of the combustion. In conclusion, within their limitations the axial microjets are an effective and reliable method of suppressing combustion instability in a backwards facing step combustor.

Bibliography

[1] L. Phares. 2005 analysis highlights of respective fe r&d program benefits. Technical report, Department of Energy, March 2006.

[2] K. C. Schadow and E. Gutmark. Combustion instability related to vortex shedding in dump combustors and their passive control. *Prog. Energy Combust. Sci.*, 18:117–132, 1991.

[3] Zheng Li Linwei Ma Hengwei Liu, Weidou Ni. Strategic thinking on igcc development in china. Technical report, Department of Thermal Engineering, Tsinghua University, 2007.

[4] L. Rayleigh. *The Theory of Sound*, volume 2, pages 224–234. Macmillan, London, 2nd edition, 1896.

[5] W. C. Strahle. On combustion generated noise. *Journal of Fluid Mechanics*, 49(2):399–414, 1971.

[6] A. P. Dowling. Instability in lean premixed combustors. *Proc, Inst. Mechanical Engineers*, 214(Part A):317–331, 2000.

[7] S. Ducruix, T. Schuller, D. Durox, and S. Candel. Combustion dynamics and instabilities: Elementary coupling and driving mechanisms. *Journal of Propulsion and Power*, 19(5):722–733, 2003.

[8] T. Lieuwen. Modeling premixed combustion-acoustic wave interactions: A review. *Journal of Propulsion and Power*, 19(5):765–781, 2003.

[9] B.T. Zinn. Pulsating combustion. *Advanced Combustion Methods*, 1986.

[10] Lord Rayleigh. The explanation of certain acoustic phenomena. *Nature*, 18:319–321, 1878.

[11] D. Bernier, F. Lacas, and S. Candel. Instability mechanisms in a premixed prevaporized combustor. *Journal of Propulsion and Power*, 20(4):648–656, 2004.

[12] K K Venkataraman, L H Preston, D W Simons, B J Lee, J G Lee, and D A Santavicca. Mechanism of combustion instability in a lean premixed dump combustor. *Journal of Propulsion and Power*, 15(6):909–918, 1999.

[13] T. J. Poinsot, A. C. Trouve, and J. W. Daily. Vortex-driven acoustically coupled combustion instabilities. *Journal of Fluid Mechanics*, 177:265–292, 1987.

[14] K. C. Schadow, E. Gutmark, T. P. Parr, D. M. Parr, K. J. Wilson, and J. E. Crump. Large-scale coherent structures as drivers of combustion instability. *Combustion Science and Technology*, 64:167–186, 1989.

[15] K. H. Poinsot, A. C. Trouve, and J. W. Daily. Low-frequency pressure oscillations in a model ramjet combustor. *Journal of Fluid Mechanics*, 232:47–72, 1991.

[16] H. N. Najm and A. F. Ghoniem. Coupling between vorticity and pressure oscillations in combustion instability. *Journal of Propulsion and Power*, 10(6):769–776, 1994.

[17] D. Thibaut and S. Candel. Numerical study of unsteady turbulent premixed combustion: Application to flashback simulation. *Combustion and Flame*, 113(1-2):53–65, 1998.

[18] C. Fureby. A computational study of combustion instabilities due to vortex shedding. *Proceedings of the Combustion Institute*, 28:783–791, 2000.

[19] Y. Huang, H. G. Sung, S. Y. Hsieh, and V. Yang. Large-eddy simulation of combustion dynamics of lean-premixed swirl-stabilized combustor. *Journal of Propulsion and Power*, 19(5):782–794, 2003.

[20] A. F. Ghoniem, A. Annaswamy, S. Park, and Z. C. Sobhani. Stability and emissions control using air injection and H_2 addition in premixed combustion. *Proceedings of the Combustion Institute*, 30:1765–1773, 2005.

[21] J. P. Hathout, M. Fleifil, A. M. Annaswamy, and A. F. Ghoniem. Heat-release actuation for control of mixture-inhomogeneity-driven combustion instability. *Proceedings of the Combustion Institute*, 28:721–730, 2000.

[22] J. G. Lee, K. Kwanwoo, and D. A. Santavicca. Measurement of equivalenceratio fluctuation and its effect on heat release during unstable combustion. *Proceedings of the Combustion Institute*, 28:415–421, 2000.

[23] T. Lieuwen, H. Torres, C. Johnson, and B.T. Zinn. A mechanism of combustion instability in lean premixed gas turbine combustors. *Journal of Engineering for Gas Turbine and Power*, 123(1):182–189, 2001.

[24] H. Santosh, Shreekrishna, and T. Lieuwen. Premixed flame response to equivalence ratio perturbations. *AIAA 2007-5656*, 2007.

[25] T. Yoshimura and V. G. McDonnell G. S. Samuelsen. Evaluation of hydrogen addition to natural gas on the stability and emissions behavior of a model gas turbine combustor. *ASME Paper GT2005-68785*, 2005.

[26] T Lieuwen, V McDonnell, E Petersen, and D Santavicca. Fuel flexibility influences on premixed combustor blowout, flashback, autoignition and stability. 2006. ASME Paper GT2006-90770.

[27] L. Figura, J. G. Lee, B. D. Quay, and D. A. Santavicca. The effects of fuel composition on flame structure and combustion dynamics in a lean premixed combustor. *ASME Paper GT2007-27298*, 2007.

[28] D M Wicksall and A K Agrawal. Acoustics measurements in a lean premixed combustor operated on hydrogen/hydrocarbon fuel mixtures. *International Journal of Hydrogen Energy*, 32:1103–1112, 2007.

[29] M.C. Janus, G. A. Richards, M. J. Yip, and E. H. Robey. Effects of ambient conditions and fuel composition on combustion stability. *ASME Paper GT97-266*, 1997.

[30] D Fritsche, M Furi, and K Boulouchos. An experimental investigation of thermoacoustic instabilities in a premixed swirl-stabilized flame. *Combustion and Flame*, 151:29–36, 2007.

[31] A. F. Ghoniem, A. M. Annaswamy, D. E. Hudgins, H. M. Altay, R. L. Speth, and D. Snarheim. Impact of microjet actuation on stability of a backward-facing step combustor. *American Institute of Aeronautics and Astronautics*, 2007.

[32] A. F. Ghoniem, H. M. Altay, D. E. Hudgins, A. M. Annaswamy, and R. L. Speth. Novel hydrocarbon-flame anchoring strategies using highly reactive fuels. 2008.

[33] Shigeru Tachibanaa, Laurent Zimmera, Yoji Kurosawab, and Kazuo Suzuki. Active control of combustion oscillations in a lean premixed combustor by secondary fuel injection coupling with chemiluminescence imaging technique. *Proceedings of the Combustion Institute*, 31:3225–3233, 2006.

[34] J.G. Lee, K. Kwanwoo, and D. A. Santavicca. Effect of injection location on the effectiveness of an active control system using secondary fuel injection. *Proceedings of the Combustion Institute*, 28:739–746, 2000.

[35] B. Higgins, M. Q. McQuay, F. Lacas, and S. Candel. An experimental study on the effect of pressure and strain rate on ch chemiluminescence of premixed fuel-lean methane-air flames. *Fuel*, (80):1583–1591, 2001.

[36] B. D. Bellows, Q. Zhang, Y. Neumeier, T. Lieuwen, and B. T. Zinn. Forced response studies of a premixed flame to flow disturbances in a gas turbine combustor. *41st AIAA Aerospace Sciences Meeting and Exhibit*, 2003.

[37] F. Ma and Y. Wang. Study on the extension of lean operation limit through hydrogen enrichment in a natural gas spark-ignition engine. *International Journal of Hydrogen Energy*, 33:1416–1424, 2008.

[38] F. Halter, C. Chauveau, and I. Gokalp. Characterization of the effects of hydrogen addition in premixed methane-air flames. *International Journal of Hydrogen Energy*, 32:2585–2592, 2007.

[39] Liu FS Ju YG Gulder OL Guo HS, Smallwood GJ. The effect of hydrogen addition on flammability limit and nox emission in ultra-lean counterflow ch4/air premixed flames. *Proceedings of the Combustion Institute*, 30:303–311, 2005.

[40] A. R. Masri, R. W. Dibble, and R. S. Barlow. The effect of hydrogen addition on flammability limit and nox emission in ultra-lean counterflow ch4-air premixed flames. *Combustion and Flame*, 91:285–309, 1992.